Filtered and Heterogeneity-Based Subgrid Modifications for Gas–Solid Drag and Solid Stresses in Bubbling Fluidized Beds

Simon Schneiderbauer and Stefan Pirker
Dept. of Particulate Flow Modelling, Johannes Kepler University, Linz, Austria

Christian-Doppler Laboratory on Particulate Flow Modelling, Johannes Kepler University, Linz, Austria

DOI 10.1002/aic.14321
Published online December 26, 2013 in Wiley Online Library (wileyonlinelibrary.com)

Two different approaches to constitutive relations for filtered two-fluid models (TFM) of gas–solid flows are deduced. The first model (Model A) is derived using systematically filtered results obtained from a highly resolved simulation of a bubbling fluidized bed. The second model (Model B) stems from the assumption of the formation of subgrid heterogeneities inside the suspension phase of fluidized beds. These approaches for the unresolved terms appearing in the filtered TFM are, then, substantiated by the corresponding filtered data. Furthermore, the presented models are verified in the case of the bubbling fluidized bed used to generate the fine grid data. The numerical results obtained on coarse grids demonstrate that the computed bed hydrodynamics is in fairly good agreement with the highly resolved simulation. The results further show that the contribution from the unresolved frictional stresses is required to correctly predict the bubble rise velocity using coarse grids. © 2013 American Institute of Chemical Engineers *AIChE J*, 60: 839–854, 2014
Keywords: bubbling fluidized bed, subgrid drag modification, subgrid stress modifications, kinetic theory-based filtered two-fluid model, coarse-grid simulations, computational fluid dynamics

Introduction

Fluidized beds are widely used in a variety of industrially important processes.[1–5] Gas-particle flows in these units are inherently unstable and are characterized by fluctuations over a wide range of time and length scales.[6] At moderate solids volume fractions, these fluctuations manifest, for example, in the random motion of particles and the formation of clusters.[7] In contrast, close to the dense packing the amount of the velocity fluctuations vanishes and heterogeneities inside gas-particle flows are triggered by strain-rate fluctuations in form of shear bands.[8]

During the last decades, the analysis of the hydrodynamics or the efficiency of fluidized beds through numerical simulations has become increasingly common.[9–12] As the total number of particles involved in most practically relevant fluidized beds is extremely large, it may be impractical to solve the equations of motion for each particle. It is, therefore, common to investigate particulate flows in large process units using averaged equations of motion.[13,14] These two-fluid model (TFM) equations take account of the behavior of the particles by considering a huge ensemble of particles and, thus, closures are required for the solids stresses arising from particle–particle contacts. However, the TFM approach requires considerably fine grids as the minimum stable sizes of clusters and shear bands are around 10 particle diameters.[8,15–19] Thus, due to computational limitations a fully resolved simulation of industrial scale reactors is still unfeasible. It is, therefore, common to use coarse grids to reduce the demand on computational resources. However, such a procedure inevitably neglects small (unresolved) scales,[20–22] which leads, for example, to a considerable overestimation of the bed expansion in the case of fine particles.[23,24]

Many subgrid drag modifications have, therefore, been put forth by academic researchers to account for the effect of small unresolved scales on the resolved meso-scales in this case.[6,25–30] Recently, the comparative study of Schneiderbauer et al.[31] revealed that although these drag modifications cited above show considerably different dependencies, they are able to predict main features of the gas and particle flow in bubbling fluidized beds adequately.

Because the magnitude of the particle stresses is much smaller than the magnitude of the drag force, only a few studies exist dealing with the unresolved part of the solids stress tensor.[6,22,26,27,32] However, Igci and Sundaresan[26] argued that neglecting their unresolved contribution produces quantitative changes in the predicted results. They also reported a significant contribution to the solids stresses arising from subgrid-scale Reynolds-stress-like velocity fluctuations in risers, which appear to be much larger than the particle stresses from kinetic theory. Recently, it has been shown that fine grid TFM simulations are able to predict these Reynolds-stress-like velocity fluctuations in risers appropriately.[7] The study of Milioli et al.[27] reveals that these fluctuations follow a Smagorinsky-like subgrid scale model. In contrast, in bubbling fluidized beds the magnitude of these subgrid-scale velocity fluctuations is still unclear. Furthermore, the study of Schneiderbauer et al.[31] demonstrates that the bubble rise velocity is considerably overestimated by coarse grid simulations even though the contribution from

Correspondence concerning this article should be addressed to S. Schneiderbauer at simon.schneiderbauer@jku.at.

the subgrid velocity fluctuations is taken into account. It appears that the dense countercurrently downflowing layer of particles around larger bubbles is not resolved adequately by the coarse grid simulation. Physically, the subgrid heterogeneities in these dense areas manifest in form of shear bands,[8] which define the smallest stable size of particle clusters in the frictional regime. This supports the demand of subgrid stress (SGS) closures at volume fractions near the closest packing accounting for the formation of subgrid shear layers.

In this article, we derive two different types of closures for the unresolved parts of the drag and the solids stresses starting from filtered numerical TFM results obtained from a bubbling fluidized bed. Following the concepts of Milioli et al.,[27] the first model (Model A) is directly deduced from the filtered data by using curve fitting. The main differences to their work are that we account for frictional stresses close to the maximum packing and that we use a bubbling fluidized bed instead of periodic domain simulations to obtain the filtered constitutive relations. The second model (Model B) is derived based on the assumption of the formation of subgrid heterogeneities inside fluidized beds. In the kinetic-collisional regime, these heterogeneities are triggered by the formation of local clusters. In contrast, in the frictional regime SGSs arise from strain-rate and volume fraction fluctuations of the solid phase at subgrid shear layer scale mainly. The latter constitutive relations are then substantiated by the filtered data. Both types of subgrid corrections are then verified in the case of a bubbling fluidized bed of fine glass particles. The numerical results are analyzed with respect to the fine grid simulation. This comparison includes the evaluation of the bed expansion, the time averaged filtered solids phase distribution with its corresponding standard deviation, the time averaged filtered particle mass fluxes, and the bubble properties including bubble size, bubble number density, and bubble rise velocities. A conclusion ends this article.

Filtered TFM Equations

As in our earlier studies,[12,31] we use a kinetic-theory-based TFM to study fluidization. We present below only the continuity, momentum, and granular temperature balance for the solid phase

$$\frac{\partial}{\partial t}\epsilon_s\rho_s+\nabla\cdot(\epsilon_s\rho_s\boldsymbol{u}_s)=0, \tag{1}$$

$$\frac{\partial}{\partial t}(\epsilon_s\rho_s\boldsymbol{u}_s)+\nabla\cdot(\epsilon_s\rho_s\boldsymbol{u}_s\boldsymbol{u}_s) =-\epsilon_s\nabla p-\nabla\cdot(\boldsymbol{\Sigma}_s^{kc}+\boldsymbol{\Sigma}_s^{fr})+\beta(\boldsymbol{u}_g-\boldsymbol{u}_s)+\epsilon_s\rho_s\boldsymbol{g}, \tag{2}$$

$$\frac{3}{2}\left(\frac{\partial}{\partial t}(\epsilon_s\rho_s\Theta)+\nabla\cdot(\epsilon_s\rho_s\boldsymbol{u}_s\Theta)\right) =-\boldsymbol{\Sigma}_s^{kc}:\nabla\boldsymbol{u}_s-\nabla\cdot\boldsymbol{q}+\Gamma_s-J_v-\gamma_\Theta. \tag{3}$$

Here, ρ_s, ϵ_s, and $\boldsymbol{u}_s$ denote density, volume fraction, and local-average velocity of the solid phase, respectively; p is the gas-phase pressure; $\boldsymbol{u}_g$ is the local-average velocity of the gas phase; β is the microscopic drag coefficient; $\boldsymbol{g}$ is the gravitational acceleration; finally, $\boldsymbol{\Sigma}_s^{kc}$ and $\boldsymbol{\Sigma}_s^{fr}$ are the stress tensors associated with the solids phase, where the frictional contribution, $\boldsymbol{\Sigma}_s^{fr}$, arises from long enduring multiple frictional contacts in dense areas. The kinetic-collisional part, $\boldsymbol{\Sigma}_s^{kc}$, is closed using kinetic theory,[12,33] which requires and additional equation for the granular temperature (Eq. 3). In Eq. 3 $-\nabla\cdot\boldsymbol{q}$ is the diffusion of the granular temperature; Γ_s and J_v represent the transfer of the kinetic energy of random fluctuations in particle velocity from the solids phase to the gas phase. The collisional dissipation, γ_Θ, represents the rate of dissipation of the granular temperature due to inelastic collisions between particles. Constitutive models used for the stresses, the Wen and Yu[34] model for the drag coefficient and the terms on the right-hand side of Eq. 3 used in our simulations can be found in Tables 3 and 4 in our previous study.[31] Thus, we will not repeat the details here.

In the case of coarse grids, it is common to use balance equations for the filtered counterparts of the local-average solids volume fraction ϵ_s and solids velocity $\boldsymbol{u}_s$. These equations can be obtained by applying a spatial filter[31] to the TFM equations 1 and 2 revealing[23,27,31] (a complete explanation of the notation is given below)

$$\frac{\partial}{\partial t}\bar{\epsilon}_s\rho_s+\nabla\cdot(\bar{\epsilon}_s\rho_s\tilde{\boldsymbol{u}}_s)=0 \tag{4}$$

for the solids continuity equation and

$$\frac{\partial}{\partial t}(\bar{\epsilon}_s\rho_s\tilde{\boldsymbol{u}}_s)+\nabla\cdot(\bar{\epsilon}_s\rho_s\tilde{\boldsymbol{u}}_s\tilde{\boldsymbol{u}}_s) =-\bar{\epsilon}_s\nabla\bar{p}-\boldsymbol{\phi}_p-\nabla\cdot\overline{\boldsymbol{\Sigma}_s^{fi}}+\tilde{\beta}(\tilde{\boldsymbol{u}}_g-\tilde{\boldsymbol{u}}_s)+\boldsymbol{\phi}_D+\rho_s\bar{\epsilon}_s\boldsymbol{g} \tag{5}$$

for the solids momentum equation with

$$\boldsymbol{\phi}_p=\overline{\epsilon_s\nabla p}-\bar{\epsilon}_s\nabla\bar{p}, \tag{6}$$

$$\boldsymbol{\phi}_D=\overline{\beta(\boldsymbol{u}_g-\boldsymbol{u}_s)}-\tilde{\beta}(\tilde{\boldsymbol{u}}_g-\tilde{\boldsymbol{u}}_s), \tag{7}$$

$$\overline{\boldsymbol{\Sigma}_s^{fi}}=\overline{\boldsymbol{\Sigma}_s^{kc}}+\overline{\boldsymbol{\Sigma}_s^{fr}}+\overline{\boldsymbol{\Sigma}_s^{R}}, \tag{8}$$

$$\overline{\boldsymbol{\Sigma}_s^{R}}=\rho_s(\overline{\epsilon_s\boldsymbol{u}_s\boldsymbol{u}_s}-\bar{\epsilon}_s\tilde{\boldsymbol{u}}_s\tilde{\boldsymbol{u}}_s), \tag{9}$$

Equations 4 and 5 have the same form as the microscopic TFM equations 1 and 2, with the phase velocities and other variables now representing filtered $\bar{\epsilon}_s$ (or Favre averaged $\tilde{\boldsymbol{u}}_s$) values. Additional terms appear that represent the unresolved part of the buoyancy, $\boldsymbol{\phi}_p$, the unresolved part of the drag, $\boldsymbol{\phi}_D$, and a Reynolds-stress-like contribution coming from the particle phase velocity fluctuations, $\boldsymbol{\Sigma}_s^R$.

The studies of Igci et al.[6] and Parmentier et al.[23] show that while in the case of bubbling fluidized beds $\boldsymbol{\phi}_p$ is negligible, $\boldsymbol{\phi}_D$ requires an adequate modeling to predict the bed expansion correctly. In the literature, it is common to model the unresolved part of drag force by[6,23,25,27,28,31]

$$\boldsymbol{\phi}_D\approx\beta^{eff}(\tilde{\boldsymbol{u}}_g-\tilde{\boldsymbol{u}}_s)-\tilde{\beta}(\tilde{\boldsymbol{u}}_g-\tilde{\boldsymbol{u}}_s)\equiv(H_D-1)\tilde{\beta}(\tilde{\boldsymbol{u}}_g-\tilde{\boldsymbol{u}}_s) \tag{10}$$

$\tilde{\beta}$ denotes the microscopic drag law computed from filtered variables. H_D is a function accounting for the unresolved structures and $\beta^{eff}\equiv H_D\tilde{\beta}$ is the effective drag coefficient due to subfilter heterogeneities. According to the EMMS group, H_D is referred to as heterogeneity index.[35] Note that for sufficiently small filter sizes, a closure for H_D should approach unity.

Compared to the magnitude of drag force, the magnitude of the particle stresses is much smaller. However, neglecting their unresolved contribution produces quantitative changes in the predicted results.[26] Especially, in this case, the rise velocity of bubbles is considerably overestimated.[31] Similar to the Boussinesq hypothesis we, therefore, propose the following model for the Reynolds-stress-like contribution[6,27]

$$\overline{\boldsymbol{\Sigma}_s^{R}}=\overline{p_s^R}\mathbf{I}-2\overline{\mu_s^R}\overline{\mathbf{S}}_s, \tag{11}$$

where $\overline{\mathbf{S}}_s$ denotes the filtered solids deviatoric rate-of-deformation tensor $\mathbf{S}_s=\mathbf{D}_s-(1/3)\mathrm{tr}(\mathbf{D}_s)$ with $\mathbf{D}_s=(\nabla\boldsymbol{u}_s+(\nabla\boldsymbol{u}_s)^T)/2$. It has to be mentioned that we do not consider

bulk viscosity effects of the Reynolds-stress-like contribution. Following Igci and Sundaresan,[26] it is reasonable to substitute the Reynolds-stress-like contribution into the kinetic-collisional part of the filtered solids stress tensor while in the frictional regime these remain negligible. Thus, we obtain

$$\overline{\boldsymbol{\Sigma}_{\mathrm{s}}^{\mathrm{fi}}}=(\overline{p_{\mathrm{s}}^{\mathrm{fi}}}+\overline{p_{\mathrm{s}}^{\mathrm{fr}}}-\overline{\lambda_{\mathrm{s}}^{\mathrm{kc}}}\,\mathrm{tr}\,(\overline{\mathbf{D}}_{\mathrm{s}}))\mathbf{I}-2(\overline{\mu_{\mathrm{s}}^{\mathrm{fi}}}+\overline{\mu_{\mathrm{s}}^{\mathrm{fr}}})\overline{\mathbf{S}}_{\mathrm{s}} \tag{12}$$

with $\overline{p_{\mathrm{s}}^{\mathrm{fi}}}=\overline{p_{\mathrm{s}}^{\mathrm{kc}}}+\overline{p_{\mathrm{s}}^{\mathrm{R}}}$ and $\overline{\mu_{\mathrm{s}}^{\mathrm{fi}}}=\overline{\mu_{\mathrm{s}}^{\mathrm{kc}}}+\overline{\mu_{\mathrm{s}}^{\mathrm{R}}}$. Thus, combining Eqs. 5, 10, and 12 yields the final form of the filtered solids momentum equation

$$\begin{aligned}&\frac{\partial}{\partial t}(\rho_{\mathrm{s}}\bar{\epsilon}_{\mathrm{s}}\tilde{\boldsymbol{u}}_{\mathrm{s}})+\boldsymbol{\nabla}\cdot(\rho_{\mathrm{s}}\bar{\epsilon}_{\mathrm{s}}\tilde{\boldsymbol{u}}_{\mathrm{s}}\tilde{\boldsymbol{u}}_{\mathrm{s}})\\&\quad=-\bar{\epsilon}_{\mathrm{s}}\boldsymbol{\nabla}\bar{p}-\boldsymbol{\nabla}\cdot\overline{\boldsymbol{\Sigma}_{\mathrm{s}}^{\mathrm{fi}}}+H_D\tilde{\beta}(\tilde{\boldsymbol{u}}_{\mathrm{g}}-\tilde{\boldsymbol{u}}_{\mathrm{s}})+\rho_{\mathrm{s}}\bar{\epsilon}_{\mathrm{s}}\boldsymbol{g},\end{aligned} \tag{13}$$

where six terms have to be closed, these are $H_D, \overline{p_{\mathrm{s}}^{\mathrm{fi}}}, \overline{p_{\mathrm{s}}^{\mathrm{fr}}}, \overline{\lambda_{\mathrm{s}}^{\mathrm{kc}}}$, $\overline{\mu_{\mathrm{s}}^{\mathrm{fi}}}$, and $\overline{\mu_{\mathrm{s}}^{\mathrm{fr}}}$.

It remains to discuss the filtered balance law for the pseudothermal energy (PTE) (Eq. 3). Defining the filtered granular temperature by $\tilde{\Theta}=\overline{\epsilon_{\mathrm{s}}\Theta}/\bar{\epsilon}_{\mathrm{s}}$ yields

$$\begin{aligned}&\frac{3}{2}\left(\frac{\partial}{\partial t}(\rho_{\mathrm{s}}\bar{\epsilon}_{\mathrm{s}}\tilde{\Theta})+\boldsymbol{\nabla}\cdot(\rho_{\mathrm{s}}\bar{\epsilon}_{\mathrm{s}}\tilde{\boldsymbol{u}}_{\mathrm{s}}\tilde{\Theta})\right)\\&\quad=-\overline{\boldsymbol{\Sigma}_{\mathrm{s}}^{\mathrm{kc}}:\boldsymbol{\nabla}\boldsymbol{u}_{\mathrm{s}}-\boldsymbol{\nabla}\cdot\boldsymbol{q}+\Gamma_{\mathrm{s}}-J_v-\gamma_\Theta}+\boldsymbol{\nabla}\cdot\overline{\boldsymbol{\theta}_{\mathrm{s}}^{\mathrm{R}}},\end{aligned} \tag{14}$$

where $\overline{\boldsymbol{\theta}_{\mathrm{s}}^{\mathrm{R}}}=(3/2)\rho_{\mathrm{s}}(\overline{\epsilon_{\mathrm{s}}\boldsymbol{u}\Theta}-\bar{\epsilon}_{\mathrm{s}}\tilde{\boldsymbol{u}}_{\mathrm{s}}\tilde{\Theta})$. In the following, we assume that the right-hand side of Eq. 14 can be modeled similar to Eqs. 10 and 12 revealing

$$\begin{aligned}\frac{3}{2}\left(\frac{\partial}{\partial t}(\rho_{\mathrm{s}}\bar{\epsilon}_{\mathrm{s}}\tilde{\Theta})+\boldsymbol{\nabla}\cdot(\rho_{\mathrm{s}}\bar{\epsilon}_{\mathrm{s}}\tilde{\boldsymbol{u}}_{\mathrm{s}}\tilde{\Theta})\right)&=-\overline{\boldsymbol{\Sigma}_{\mathrm{s}}^{\mathrm{kc}}:\boldsymbol{u}_{\mathrm{s}}}-\boldsymbol{\nabla}\cdot\overline{\boldsymbol{q}^{\mathrm{fi}}}+\bar{\Gamma}_{\mathrm{s}}\\&\quad-\bar{J}_v-\bar{\gamma}_\Theta,\end{aligned} \tag{15}$$

where closures for the terms on the right-hand side are required. We found that for not too large filter lengths $\bar{G}_\Theta=-\overline{\boldsymbol{\Sigma}_{\mathrm{s}}^{\mathrm{kc}}:\boldsymbol{u}_{\mathrm{s}}}\approx-\overline{\boldsymbol{\Sigma}_{\mathrm{s}}^{\mathrm{kc}}}:\tilde{\boldsymbol{u}}_{\mathrm{s}}\ (\equiv\tilde{G}_\Theta)$, $\bar{\Gamma}_{\mathrm{s}}\approx H_D^{3/2}\tilde{\Gamma}_{\mathrm{s}}, \bar{J}_v\approx 3\tilde{\beta}\tilde{\Theta}$ and $\bar{\gamma}_\Theta\approx\tilde{\gamma}_\Theta$, which we will verify in the next chapter. Here, $\tilde{\Gamma}_{\mathrm{s}}$ and $\tilde{\gamma}_\Theta$ denote the production of PTE due to gas-particle slip and the dissipation of PTE due to interparticle collisions computed from filtered variables, respectively.

Fine Grid Simulation and Results

To study the contribution of the unresolved term appearing in Eq. 13 in the bubbling regime, we investigated a gas-solid fluidized bed of Geldart type B glass particles using a superficial gas velocity $W_{\mathrm{g}}^{\mathrm{in}}=0.22u_t$, where $u_t=0.96\mathrm{ms}^{-1}$ is the terminal settling velocity. This case has also been presented in our previous study (Figure 4 and Table 2 of Schneiderbauer et al.[31]) and thus, we will not repeat all the details here. We obtained a time-dependent solution using a grid spacing $\hat{\Delta}=0.9$, which is assumed to be sufficiently fine to resolve all heterogeneous structures.[18,31] Note that we made the grid spacing Δ and the filter size Δ_{f} dimensionless by a characteristic length scale for the heterogenous structures $\mathbb{L}_{\mathrm{ch}}$[36]

$$\mathbb{L}_{\mathrm{ch}}=\frac{u_t^2}{g}\mathrm{Fr}^{-2/3}\approx 9d_{\mathrm{s}}, \tag{16}$$

where $\mathrm{Fr}=u_t^2/d_{\mathrm{s}}g$ denotes the particle-based Froude number and $d_{\mathrm{s}}=150\mu\mathrm{m}$ is the particle diameter. The simulations were started from a slightly nonuniform settled state to expedite the development of inhomogeneous flow structures, such as bubbles. After an initial transient period, that is, the expansion of the bed, the system reached a statistical steady state with persistent temporally and spatially distributed bubbles. A detailed discussion of the features of the solids flow can be found in our previous study[31] and are also discussed later. In this section, we restrict ourselves to the discussion of filtered quantities. Following previous work,[6,23,26,27] snapshots of the flow field were collected at various times after the initialization phase. These computational data were then filtered using filters of different sizes. By this procedure we collected, for example, about 15 million data points for a filter size of $\hat{\Delta}_{\mathrm{f}}=3.74$. Finally, the filtered data were binned in terms of the values of the markers used to classify the subfilter scale state and averaged to obtain statistics of the filtered quantities. The filtered quantities will be presented in dimensionless form, that is

$$\begin{aligned}&\hat{\overline{p_{\mathrm{s}}^{\mathrm{i}}}}=\frac{\overline{p_{\mathrm{s}}^{\mathrm{i}}}}{\rho_{\mathrm{s}}u_t^2},\ \hat{\overline{\mu_{\mathrm{s}}^{\mathrm{i}}}}=\frac{\overline{\mu_{\mathrm{s}}^{\mathrm{i}}}g}{\rho_{\mathrm{s}}u_t^3},\ \hat{\overline{\mathbf{S}}}_{\mathrm{s}}=\overline{\mathbf{S}}_{\mathrm{s}}\frac{u_t}{g},\ \hat{\widetilde{W}}_{\mathrm{g}}=\frac{\widetilde{W}_{\mathrm{g}}}{u_t},\ \hat{\bar{G}}_\Theta=\frac{\bar{G}_\Theta}{3/2\rho_s u_t g},\\&\hat{\bar{\gamma}}_\Theta=\frac{\bar{\gamma}_\Theta}{3/2\rho_s u_t g},\ \hat{\bar{\Gamma}}_{\mathrm{s}}=\frac{\bar{\Gamma}_{\mathrm{s}}}{3/2\rho_{\mathrm{s}}u_t g},\ \hat{\bar{J}}_v=\frac{\bar{J}_v}{3/2\rho_{\mathrm{s}}u_t g}\end{aligned} \tag{17}$$

with $\mathrm{i}\in\{\mathrm{fi},\mathrm{kc},\mathrm{fr},\mathrm{R}\}$. Here, $\rho_{\mathrm{s}}u_t^2$ defines a characteristic stress, $\rho_{\mathrm{s}}u_t^3/g$ is the characteristic stress times a characteristic time and $3/2\rho_{\mathrm{s}}u_t g$ is a characteristic power.

The heterogeneity index, H_D, can be computed as follows from the filtered data

$$H_D=\frac{\overline{\beta^{\mathrm{fi}}}}{\tilde{\beta}}\quad\text{with}\quad\overline{\beta^{\mathrm{fi}}}=\frac{\|\overline{\beta(\boldsymbol{u}_{\mathrm{g}}-\boldsymbol{u}_{\mathrm{s}})}\|}{\|\tilde{\boldsymbol{u}}_{\mathrm{g}}-\tilde{\boldsymbol{u}}_{\mathrm{s}}\|} \tag{18}$$

where, $\overline{\beta^{\mathrm{fi}}}$ is the filtered drag coefficient and $\tilde{\beta}$ denotes the microscopic drag coefficient computed from filtered quantities. Note that $\overline{\beta^{\mathrm{fi}}}$ can be used to find closure relations for the effective drag coefficient appearing in Eq. 10. The heterogeneity index, H_D, is a measure of the subgrid heterogeneity. Thus, small values of H_D indicate more developed subfilter heterogeneity than values near 1. In contrast to Milioli et al.,[27] we did not substitute the contribution from the gas pressure gradient fluctuations into the definition of H_D as these appear to be negligible in bubbling fluidized beds.[23] According to Milioli et al.,[27] the markers for the heterogeneity index are the filtered void fraction $\bar{\epsilon}_{\mathrm{g}}$ and the dimensionless slip velocity $\hat{\tilde{u}}_{\mathrm{sg}}=\|\tilde{\boldsymbol{u}}_{\mathrm{g}}-\tilde{\boldsymbol{u}}_{\mathrm{s}}\|/u_t$. In Figure 1, the variation of H_D with the filtered void fraction for different slip velocities and different filter sizes is plotted. The figure shows that compared to the microscopic drag coefficient $\tilde{\beta}$, the filtered drag coefficient $\overline{\beta^{\mathrm{fi}}}$ is considerably reduced for a wide range of void fractions. Solely in very dilute regions ($\bar{\epsilon}_{\mathrm{g}}\to 1$) and in very dense regions, that is, close to the maximum packing ($\bar{\epsilon}_{\mathrm{g}}\to 1-\epsilon_{\mathrm{s}}^{\max}$), no subfilter heterogeneities evolve. As reported by several authors,[6,23,26,27] H_D decreases with increasing filter length, while this trends gets less pronounced for larger filter lengths. Similar to the results of Milioli et al.,[27] we observe that H_D decreases with increasing slip velocity, since at higher slip velocities the subfilter structures appear to be more heterogenous. For high slip velocities, the figure also reports an asymptotic behavior of H_D at large filters, which appears to be at considerably

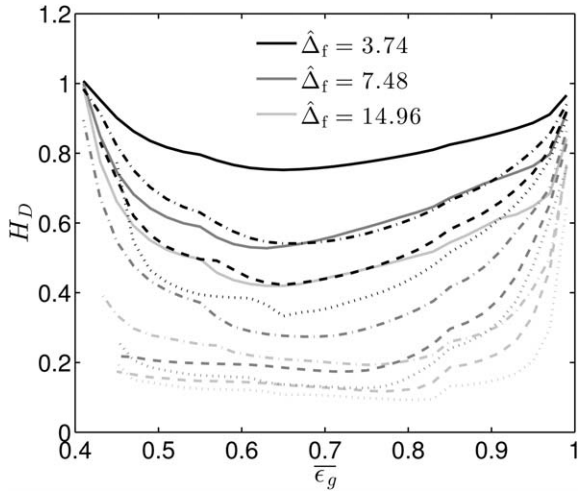

Figure 1. Variation of H_D with the filtered void fraction, $\bar{\epsilon}_g$, for different dimensionless filter sizes $\hat{\Delta}_f = \Delta_f/\mathbb{L}_{ch}$ and different dimensionless slip velocities $\hat{\tilde{u}}_{gs}$: — $\hat{\tilde{u}}_{gs}=0.25$; – · – $\hat{\tilde{u}}_{gs}=0.75$; – – – $\hat{\tilde{u}}_{gs}=1.25$; · · · $\hat{\tilde{u}}_{gs}=1.75$.

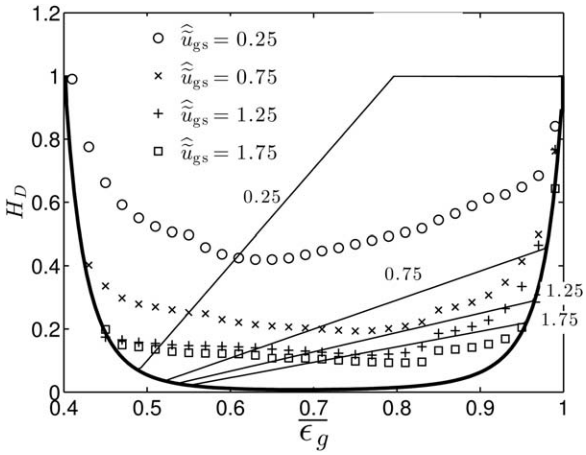

Figure 3. Variation of H_D with the filtered void fraction, $\bar{\epsilon}_g$, for a dimensionless filter size $\hat{\Delta}_f=14.96$ and different dimensionless slip velocities $\hat{\tilde{u}}_{gs}$.

The thick solid line indicates the envelop of H_D, that is, H_D at large filters and high slip velocities. The thin solid lines represent the model of Milioli et al.[27]

smaller filter lengths than for low slip velocities. Near the maximum packing, the figure reveals that solely small slip velocities are present, as most of the gas flows through regions of less drag, that is, through voids or bubbles.

Figure 1 further indicates that H_D is confined to [0,1]. This is indeed true for the values of H_D, which are deduced from averaging a huge number of realizations of H_D with identical $\bar{\epsilon}_s$ and $\hat{\tilde{u}}_{gs}$. Unlike that observation, Figure 2 clearly shows that H_D may also exceed 1. This gives indication to an additional marker for H_D. However, as those events are very rare we do not discuss $H_D > 1$ in more detail. Finally, Figure 2 further reveals that very dilute and very dense areas are observed most frequently, as in bubbling fluidized beds dilute bubbles and dense regions prevail.

In Figure 3, a comparison of the residual correlations for H_D of Milioli et al.[27] with our data at large filter lengths is shown. Their study revealed that H_D can be modeled by the maximum of the envelop of H_D and a linear function, where the linear function pictures the dependence on the slip velocity. Although linear regions can also be identified from our data as well (e.g., H_D shows nearly linear behavior between $0.45 < \bar{\epsilon}_g < 0.85$ for $\hat{\tilde{u}}_{gs}=1.25$ and $\hat{\tilde{u}}_{gs}=1.75$), their slopes appear considerably different to those from Milioli et al. Furthermore, our data shows that heterogenous structures develop even for small slip velocities ($\hat{\tilde{u}}_{gs}=0.25$) over a wide range of solids volume fractions, which is not observed in their study. These differences may originate from the different physical conditions. Although Milioli et al.[27] do not account explicitly for long enduring multiple frictional contacts close to the maximum packing, we apply an inertial number dependent rheology instead of using kinetic theory for the whole range of solids volume fractions.[12,31] Their work also uses periodic domain simulations of a riser-like flow to gather the fine grid data, whereas in our study, a bubbling fluidized bed is studied to collect the filtered data. In addition, H_D also depends on other markers than the filtered solids volume fraction and the filtered slip velocity; for example, the effective drag monotonically decreases with an increasing kinetic energy of the subfilter scale velocity fluctuations $k=(1/2)\widetilde{\boldsymbol{u}_s''\boldsymbol{u}_s''}$ (not shown here; $\boldsymbol{u}''=\boldsymbol{u}-\tilde{\boldsymbol{u}}$). In general, k scales with $\rho_s u_t^2$ implying an approximately 20 times higher energy of the subfilter scale velocity fluctuations in our case than in the study of Milioli et al.[27] ($u_t^{\text{Milioli}} = 0.218\text{ms}^{-1}$). Thus, an additional dependence of H_D on k may be used to explain the differences shown in Figure 3. However, in a first step, we discuss the dependence of H_D on those markers proposed by Milioli et al.[27] only. To conclude, both studies reveal similar trends, these are, H_D decreases with increasing filtered slip velocity, and H_D decreases with increasing filter size (not shown here). Finally, both predict an asymptotic limit at high filtered slip velocities and large filter lengths, which is indicated by the envelop in Figure 3.

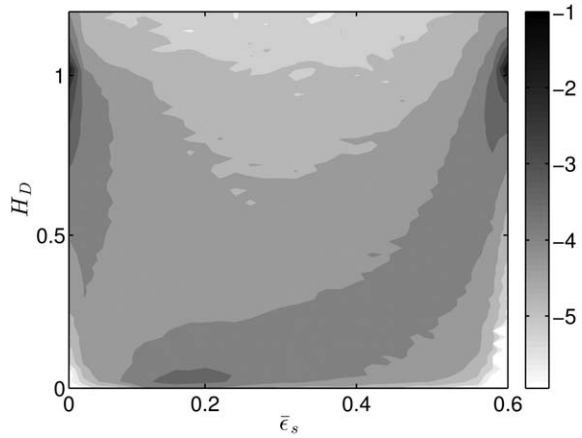

Figure 2. Logarithmic grayscale plot of the relative frequencies of H_D as a function of the filtered solids volume fraction, $\bar{\epsilon}_s$, for a dimensionless filter sizes $\hat{\Delta}_f=7.48$.

In Figure 4, the different contributions to the dimensionless filtered solids pressure, $\overline{p_s^{fi}}$, and the dimensionless filtered solids shear viscosity, $\overline{\mu_s^{fi}}$, are plotted, respectively. Note that the contributions from the Reynolds-stress-like velocity fluctuations can be computed from

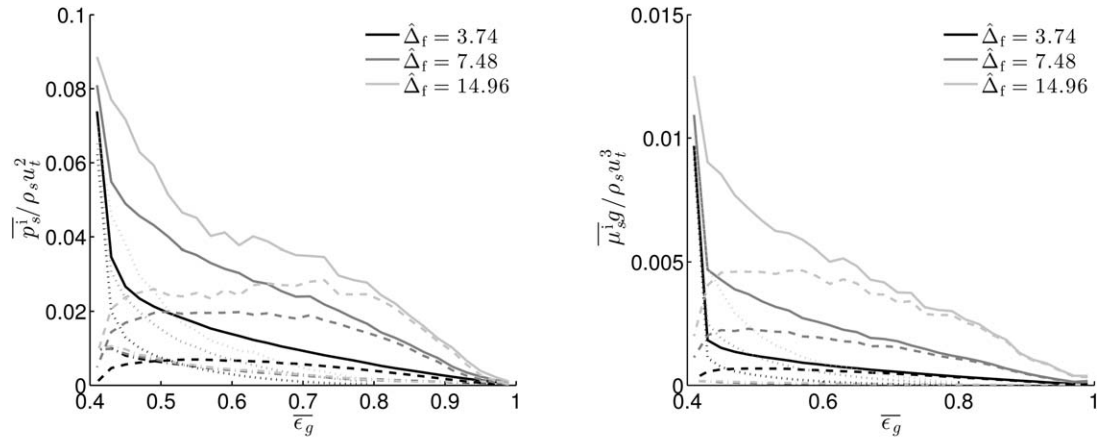

Figure 4. Variation of (a) $\hat{\overline{p_s^i}}$ and (b) $\hat{\overline{\mu_s^i}}$ with the filtered void fraction, $\bar{\epsilon}_g$, for different dimensionless filter sizes $\hat{\Delta}_f$: — $\hat{\overline{p_s^{fi}}}, \hat{\overline{\mu_s^{fi}}}$; – · – $\hat{\overline{p_s^{kc}}}, \hat{\overline{\mu_s^{kc}}}$; – – – $\hat{\overline{p_s^R}}, \hat{\overline{\mu_s^R}}$; · · · $\hat{\overline{p_s^{fr}}}, \hat{\overline{\mu_s^{fr}}}$.

$$\hat{\overline{p_s^R}} = \frac{1}{3}\frac{\mathrm{tr}\,(\overline{\boldsymbol{\Sigma}_s^R})}{\rho_s u_t^2}, \tag{19}$$

$$\hat{\overline{\mu_s^R}} = \frac{\|\overline{\boldsymbol{\Sigma}_s^R} - \overline{p_s^R}\mathbf{I}\|}{2\|\hat{\overline{\mathbf{S}}}_s\|\rho_s u_t^2} \tag{20}$$

with $\|\hat{\overline{\mathbf{S}}}_s\| = \sqrt{\hat{\overline{\mathbf{S}}}_s : \hat{\overline{\mathbf{S}}}_s/2}$. The figure clearly shows that in dilute regions the solids stresses are dominated by the contribution form the Reynolds-stress-like velocity fluctuations (R), while the contribution from the filtered kinetic-collisional contribution (kc) appears to be negligible for larger filter lengths. This was also observed by other authors.[6,26] In more dense regions, that is, $\bar{\epsilon}_g < 0.7$, our data confirms that the contribution form the filtered frictional stresses shows a nonnegligible contribution. Especially, close to the maximum packing both, the filtered solids pressure and the filtered solids shear viscosity, are determined by the frictional part. According to Milioli et al.,[27] $\overline{p_s^{fi}}$ and $\overline{\mu_s^{fi}}$ do not reveal a systematic dependence on $\hat{\tilde{u}}_{gs}$ while both appear to depend considerably on the square of the scalar shear rate $4\|\overline{\mathbf{S}}_s\|^2$. Our data reveals identical dependencies, which we will discuss later.

Figures 5 and 6 show the variation of the production of the filtered generation of PTE due to the solids pressure $\hat{\overline{G_\Theta^p}}$ ($\equiv \hat{\overline{-p_s^{kc}\,\mathrm{tr}\,(\mathbf{D}_s)}}$; note that we solely consider the production due to the solids pressure as an example to discuss the subgrid contribution to the production of PTE), the filtered dissipation of PTE $\hat{\bar{\gamma}}_\Theta$, the filtered viscous damping of PTE $\hat{\bar{J}}_v$, and the filtered production of PTE due to gas-particle slip $\hat{\bar{\Gamma}}_s$ with the filtered void fraction $\bar{\epsilon}_g$. Remarkably, the Figure 5 reveals that $\hat{\bar{J}}_v \approx \hat{\tilde{J}}_v$ and, therefore, no drag correction applies to the viscous damping term. In contrast, the production term $\hat{\bar{\Gamma}}_s$ obviously requires a drag modification term in the form of $H_D^n \hat{\tilde{\Gamma}}_s$. The figure yields that $n \approx 3/2$. Even though $\hat{\bar{J}}_v$ and $\hat{\bar{\Gamma}}_s$ can be computed from the filtered variables (these are $\tilde{\beta}, \tilde{\Theta}, \bar{\epsilon}_s$, and $\tilde{u}_{gs}$), Figure 6 demonstrates that $\hat{\overline{G_\Theta^p}}$ and $\hat{\bar{\gamma}}_\Theta$ may not be evaluated in this manner at larger filter lengths and closures for these terms may be required. However, it appears that the subgrid contributions to $\hat{\overline{G_\Theta^p}}$ and $\hat{\bar{\gamma}}_\Theta$ are negligible in dilute and very dense areas and,

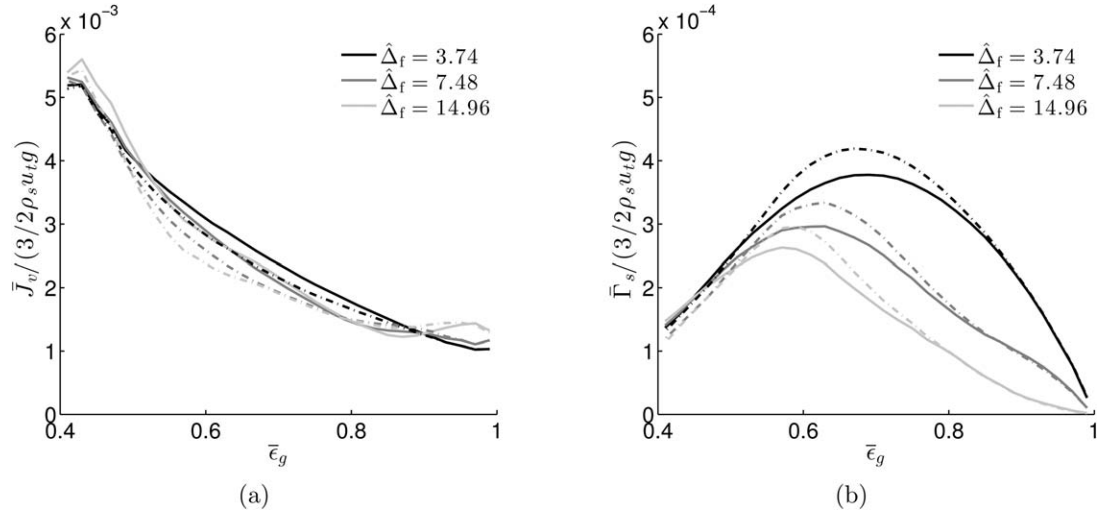

Figure 5. Variation of (a) $\hat{\bar{J}}_v$ and (b) $\hat{\bar{\Gamma}}_s$ with the filtered void fraction, $\bar{\epsilon}_g$, for different dimensionless filter sizes $\hat{\Delta}_f$: — filtered data; – · – (a) $\hat{\tilde{J}}_v = 3\tilde{\beta}\tilde{\Theta}/(3/2\rho_s u_t g)$, (b) $H_D^{3/2}\hat{\tilde{\Gamma}}_s$.

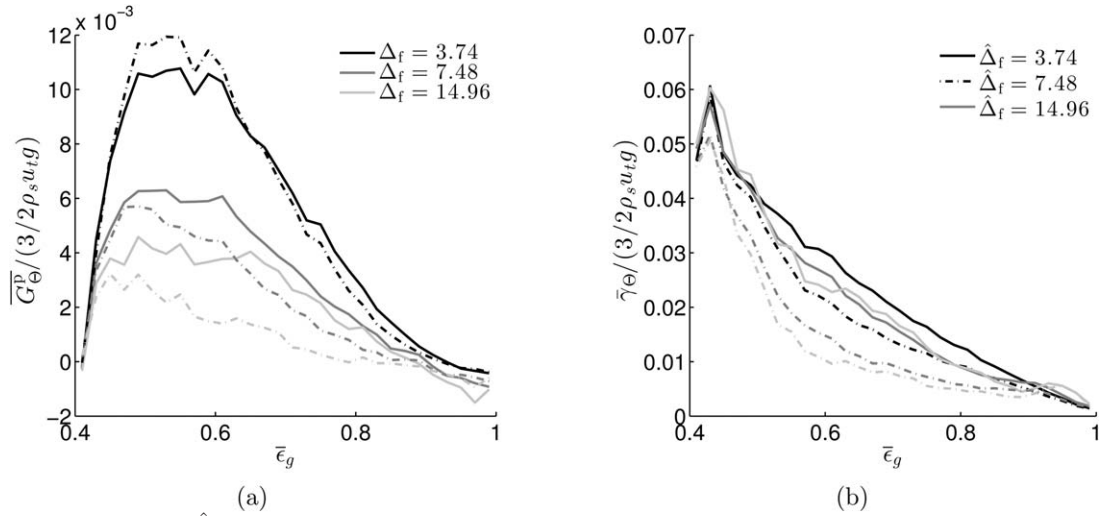

Figure 6. Variation of (a) $\widehat{\overline{G_\Theta^p}}$ and (b) $\hat{\bar{\gamma}}_\Theta$ with the filtered void fraction, $\bar{\epsilon}_g$, for different dimensionless filter sizes $\hat{\Delta}_f$: — filtered data; – · – (a) $G_\Theta^p = -\overline{p_s^{kc}}\,\mathrm{tr}(\overline{\mathbf{D}}_s)/(3/2\rho_s u_t g)$, (b) $\hat{\bar{\gamma}}_\Theta$.

therefore, it is reasonable to evaluate both terms using filtered variables in bubbling fluidized beds, where intermediate solids volume fractions occur very rarely. Thus, we do not discuss subgrid corrections of $\widehat{\overline{G_\Theta^p}}$ and $\hat{\bar{\gamma}}_\Theta$ further in a first step. The figures further yield that $\hat{\bar{\Gamma}}_s$ and $\widehat{\overline{G_\Theta^p}}$ show a considerable dependence on the filter length, while $\hat{\bar{\gamma}}_\Theta$ and $\hat{\bar{J}}_v$ appear nearly unaffected by varying filter size. Finally, it has to be noted that $\hat{\bar{J}}_v$ and $\hat{\bar{\Gamma}}_s$ are at least one order of magnitude smaller than $\hat{\bar{\gamma}}_\Theta$ and seem, therefore, negligible in coarse grid simulations of bubbling fluidized beds.

In the following, we present two different types of subgrid modifications for the unclosed terms in Eqs. 13 and 15 showing nonnegligible unresolved contributions. The first type of closure models follows Mililoli et al.[27] by least-squares fits of the filtered data. The latter approach is deduced from the assumption of the formation of subgrid clusters and shear layers.

Filtered Subgrid Modifications (Model A)

Constitutive relation for filtered drag

In this study, we propose that the filtered data of H_D can be correlated with

$$H_D = H_{\epsilon_s,\Delta}(\bar{\epsilon}_s, \hat{\Delta}_f) H_u(\bar{\epsilon}_s, \hat{\tilde{u}}_{gs}, \hat{\Delta}_f) \tag{21}$$

where $H_{\epsilon_s,\Delta}(\bar{\epsilon}_s, \hat{\Delta}_f)$ represents the influence of the filtered solids volume fraction, $\bar{\epsilon}_s$, and the dimensionless filter length, $\hat{\Delta}_f$. Several authors[6,23,26] proposed that $H_{\epsilon_s,\Delta}$ can be written as

$$H_{\epsilon_s,\Delta}(\bar{\epsilon}_s, \hat{\Delta}_f) = 1 - h_\epsilon(\bar{\epsilon}_s) h_\Delta(\hat{\Delta}_f) \tag{22}$$

where h_ϵ and h_Δ are solely functions of $\bar{\epsilon}_s$ and $\hat{\Delta}_f$, respectively. Furthermore, $H_u(\bar{\epsilon}_s, \hat{\tilde{u}}_{gs}, \hat{\Delta}_f)$ (Eq. 21) includes the dependence on the dimensionless filtered slip velocity. From the data, it is observed that H_u depends on all three markers for H_D, these are $\bar{\epsilon}_s$, $\hat{\tilde{u}}_{gs}$, and $\hat{\Delta}_f$ and that H_u take the following form

$$H_u(\bar{\epsilon}_s, \hat{\tilde{u}}_{gs}, \hat{\Delta}_f) = (\hat{\tilde{u}}_{gs})^{-c f_u^\Delta(\hat{\Delta}_f) f_u^\epsilon(\bar{\epsilon}_s)} \tag{23}$$

with

$$c \approx 9 \tag{24}$$

$$f_u^\epsilon(\bar{\epsilon}_s) = \bar{\epsilon}_s(\epsilon_s^{max} - \bar{\epsilon}_s). \tag{25}$$

$$f_u^\Delta(\hat{\Delta}_f) = \frac{\hat{\Delta}_f^5}{\hat{\Delta}_f^5 + 1024} \tag{26}$$

where f_u^Δ introduces a large filter limit for H_u (see discussion in previous section, Figures 1 and 3).

In Figure 7, the variation of the ratio between H_D and H_u with the filtered void fraction $\bar{\epsilon}_g$ is plotted. The figure yields that the curves for different slip velocities collapse by using Eq. 23. Furthermore, we propose that h_ϵ and h_Δ can be described by

$$h_\epsilon(\hat{\bar{\epsilon}}_s) = \frac{p_1 \hat{\bar{\epsilon}}_s^2 + p_2 \hat{\bar{\epsilon}}_s + p_3}{\hat{\bar{\epsilon}}_s^3 + q_1 \hat{\bar{\epsilon}}_s^2 + q_2 \hat{\bar{\epsilon}}_s + q_3} \tag{27}$$

and

$$h_\Delta(\hat{\Delta}_f) = \frac{\hat{\Delta}_f^a}{\hat{\Delta}_f^a + b} \tag{28}$$

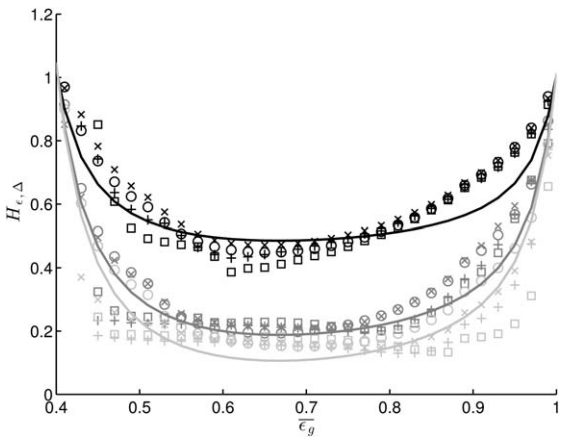

Figure 7. Variation of $H_D/H_u = H_{\epsilon_s,\Delta}$ with the filtered void fraction, $\bar{\epsilon}_g$, for different filter sizes Δ_f: ○ $\hat{\tilde{u}}_{gs} = 0.25$; × $\hat{\tilde{u}}_{gs} = 0.75$; + $\hat{\tilde{u}}_{gs} = 1.25$; □ $\hat{\tilde{u}}_{gs} = 1.75$.

The solid lines correspond to fits using Eqs. 22, 27, and 28. The colors of the lines and symbols have the same meaning as in figure 1.

Table 1. Numerical Values of the Coefficients Appearing in Eqs. 27 and 28, which were Determined from Least-Squares Fits using Eqs. 27 and 28 (R^2=0.98)

Coefficient	Value
P_1	−6.743
P_2	6.728
p_3	0
q_1	−7.247
q_2	6.289
q_3	0.384
a	2.664
b	25.89

with $\hat{\bar{\epsilon}}_s=\bar{\epsilon}_s/\epsilon_s^{max}$, respectively. The coefficients appearing in Eqs. 27 and 28, which we determined from least-squares fits, are given in Table 1. In Figure 7, the curve fits for $H_{\epsilon_s,\Delta}$ are plotted for different filter lengths, Δ_f, yielding reasonable agreement with its corresponding filtered data.

Figure 8 shows a comparison of the filtered data of H_D with the curve fits (Eq. 21) yielding that Eq. 21 describes the filtered data reasonably well for a wide range of filter lengths and filtered void fractions. Especially, for large filters the predictions of Eq. 21 are in fairly good agreement with the filtered data. Note that at small filter length ($\hat{\Delta}_f=3.74$) and low slip velocities ($\hat{\tilde{u}}_{gs}=0.25$) Eq. 21 disagrees with the filtered data, which, in turn, may be attributed to the form of $H_{\epsilon,\Delta}$. However, the presented fits lie within the standard deviation of the statistical fine grid data for the presented filter lengths and the whole range of solids volume fractions.

Constitutive relations for filtered stresses

The results of Schneiderbauer et al.[31] indicate that coarse grid simulations, which only consider the effect of subgrid heterogeneities in the fluid to solid phase drag, considerably overestimate the bubble rise velocity. The solids stress tensor basically consists of two different contributions (kinetic-collisional and frictional parts), which are characterized by different behavior of the interparticle contacts. Although in the collisional regime the interparticle collisions can be treated as binary, the particle–particle interactions in the frictional regime are dominated by long enduring frictional contacts. In the collisional regime, a nonnegligible contribution from Reynolds-stress-like velocity fluctuations requires additional subgrid modeling using coarse grids (Figure 4). Even though accounting for the Reynolds-stress-like velocity fluctuations does not improve the estimation of bubble rise velocity.[31] Thus, the unresolved part of the frictional particle stresses has to be considered in bubbling fluidized beds. In particular, in dense regions the contribution stemming from the velocity fluctuations appears negligible, while the stresses are determined by the filtered frictional stresses (Figure 4).

Table 2. Summary of Filtered Subgrid Modifications (Model A)

1. Filtered drag coefficient

$$\beta^{\text{eff}}=\left(1-h_\epsilon(\hat{\bar{\epsilon}}_s)h_\Delta(\hat{\Delta}_f)\right)H_u(\bar{\epsilon}_s,\hat{\tilde{u}}_{gs},\hat{\Delta}_f)\tilde{\beta}$$

$$H_u(\bar{\epsilon}_s,\hat{\tilde{u}}_{gs},\hat{\Delta}_f)=(\hat{\tilde{u}}_{gs})^{-9\bar{\epsilon}_s(\epsilon_s^{max}-\bar{\epsilon}_s)\hat{\Delta}_f^5/(\hat{\Delta}_f^5+1024)}$$

$$h_\epsilon(\hat{\bar{\epsilon}}_s)=\frac{-6.743\hat{\bar{\epsilon}}_s^2+6.728\hat{\bar{\epsilon}}_s}{\hat{\bar{\epsilon}}_s^3-7.247\hat{\bar{\epsilon}}_s^2+6.289\hat{\bar{\epsilon}}_s+0.384}\ \text{with}\ \hat{\bar{\epsilon}}_s=\bar{\epsilon}_s/\epsilon_s^{max}$$

$$h_\Delta(\hat{\Delta}_f)=\frac{\hat{\Delta}_f^{2.664}}{\hat{\Delta}_f^{2.664}+25.89}$$

2. Filtered particle phase normal stress

$$\frac{\overline{p_s^{fi}}}{\rho_s u_t^2}=4C_p'\text{Fr}^{-31/21}\hat{\Delta}_f^{16/7}||\hat{\bar{\mathbf{S}}}_s||^2\qquad C_p'=0.17\bar{\epsilon}_s+\frac{0.0235\bar{\epsilon}_s}{\epsilon_s^{max}(\epsilon_s^{max}-\bar{\epsilon}_s)^{3/4}}$$

3. Filtered particle phase shear viscosity

$$\frac{\overline{\mu_s^{fi}}\,g}{\rho_s u_t^3}=4C_\mu'\text{Fr}^{-4/3}\hat{\Delta}_f^2||\hat{\bar{\mathbf{S}}}_s||\qquad C_\mu'=0.105\bar{\epsilon}_s+\frac{0.001\bar{\epsilon}_s}{\epsilon_s^{max}(\epsilon_s^{max}-\bar{\epsilon}_s)}$$

By inspiration from single-phase turbulence literature,[37] Milioli et al.[27] proposed Smagorinsky-like constitutive models for the filtered solids pressure and filtered solids shear viscosity, which can be written as follows

$$\begin{aligned}\overline{\hat{p_s^{fi}}}&=4C_p(\bar{\epsilon}_s)\text{Fr}^{-31/21}\hat{\Delta}_f^{16/7}||\hat{\bar{\mathbf{S}}}_s||^2,\\ \overline{\hat{\mu_s^{fi}}}&=4C_\mu(\bar{\epsilon}_s)\text{Fr}^{-4/3}\hat{\Delta}_f^2||\hat{\bar{\mathbf{S}}}_s||,\end{aligned}\tag{29}$$

with the effective pressure and viscosity coefficients

$$C_p(\bar{\epsilon}_s)=0.17\bar{\epsilon}_s\quad\text{and}\quad C_\mu(\bar{\epsilon}_s)=0.105\bar{\epsilon}_s.\tag{30}$$

Note that they used a different scaling for the filter length, that is $\check{\Delta}_f=\Delta_f g/u_t^2$. It is further noteworthy that Eq. 29 renders a transport equation for the PTE (Eq. 15) unnecessary as those constitutive relations solely depend on the filtered solids volume fraction and the filtered solids shear rate. Finally, it has to be mentioned that we do not consider bulk viscosity effects in this filtered model.

In Figure 9, Eq. 29 is compared with the filtered data of the solids pressure, $\overline{\hat{p_s^{fi}}}$ and the solids shear viscosity, $\overline{\hat{\mu_s^{fi}}}$ (compare also with Figure 4). Remarkably, Eq. 29 is in fairly good agreement as $\bar{\epsilon}_g$ tends to 1 with the filtered results even though those equations were derived for Geldart type A particles. Thus, we conclude that for the fluidization of Geldart type B particles identical markers for the filtered solids stresses apply as identified by the study of Milioli et al.[27] (these are $\hat{\Delta}_f$ and $||\hat{\bar{\mathbf{S}}}_s||$). In intermediate and dense areas, where the filtered frictional stresses start to become nonnegligible (Figure 4), Eq. 29 considerably underestimates the filtered data, as their fine grid simulations considered frictional stresses solely very close to the maximum packing. However, our previous study[12] has shown that frictional stresses indeed become important even at significantly smaller solids volume fractions ($\epsilon_s>0.4$). Especially, these stresses are essential to reasonably predict the gas-solid flow in dense fluidized beds and hoppers.[12,38,39] From the filtered data, we find that the filtered frictional stresses can be taken into account by the following modification of the effective pressure and viscosity coefficients

Table 3. Summary of Heterogeneity-Based Subgrid Modifications (Model B)

1. Heterogeneity-based subgrid drag coefficient[31]

$$\tilde{\beta}^{\text{CL}}=\frac{1}{||\tilde{\boldsymbol{u}}_g-\tilde{\boldsymbol{u}}_s||}\|\boldsymbol{F}_d^{\text{cl}}+f^c\boldsymbol{F}_d^c\|$$

2. Heterogeneity-based particle phase normal stresses

$$\overline{p_s^{fi}}=\bar{\epsilon}_s\rho_s\left(\frac{1}{1+l_s/\mathbb{L}}+4\eta_s\epsilon_s^c g_0^c\right)\tilde{\Theta}+\bar{\epsilon}_s\rho_s\Theta^{\text{cl}}$$

$$\text{with}\quad\Theta^{\text{cl}}=0.15\sqrt{\frac{\epsilon_s^c}{\epsilon_s^{max}}}\left(\frac{d_{cl}}{d_s}\right)^2\tilde{\Theta}$$

$$\overline{p_s^{fr}}=\frac{10d_s}{\Delta}\sum_{k=1}^{10d_s/\Delta}p_s^{fr}(\epsilon_{s,k},||\mathbf{S}_{s,k}||)\quad\text{(compare with Eq. 45)}$$

Closures for ϵ_s^c and d_{cl} are given in our previous study.[31]

3. Heterogeneity-based particle phase shear viscosities

$$\overline{\mu_s^{fi}}=\frac{6}{5}\left\{\frac{f^c\mu^*}{g_0^c\eta_s(2-\eta_s)}\left(\frac{1}{1+\frac{l_s}{\mathbb{L}}}+\frac{8}{5}\epsilon_s^c\eta_s g_0^c\right)(1+\frac{8}{5}\eta_s(3\eta_s-2)\epsilon_s^c g_0^c)+\frac{3}{5}\eta_s\mu_b^c\right\}+\overline{\mu_s^R}$$

where

$$\overline{\mu_s^R}=\bar{\epsilon}_s\rho_s d_{\text{cl}}\sqrt{\Theta^{\text{cl}}},\ \mu_c^c=\frac{8}{3}\bar{\epsilon}_s\rho_s\sqrt{\frac{\tilde{\Theta}}{\pi}}\epsilon_s^c d_s g_0^c,\ \mu^*=\frac{\mu}{1+\frac{2\tilde{\beta}^{\text{CL}}\mu}{(\epsilon_s^c\rho_s)^2 g_0^c\tilde{\Theta}}},\ \mu=\frac{5\rho_s d_s\sqrt{\pi\tilde{\Theta}}}{96}$$

$$\overline{\mu_s^{fr}}=\frac{10d_s}{\Delta}\sum_{k=1}^{10d_s/\Delta}\mu_s^{fr}(\epsilon_{s,k},||\mathbf{S}_{s,k}||)\quad\text{(compare with Eq. 46)}$$

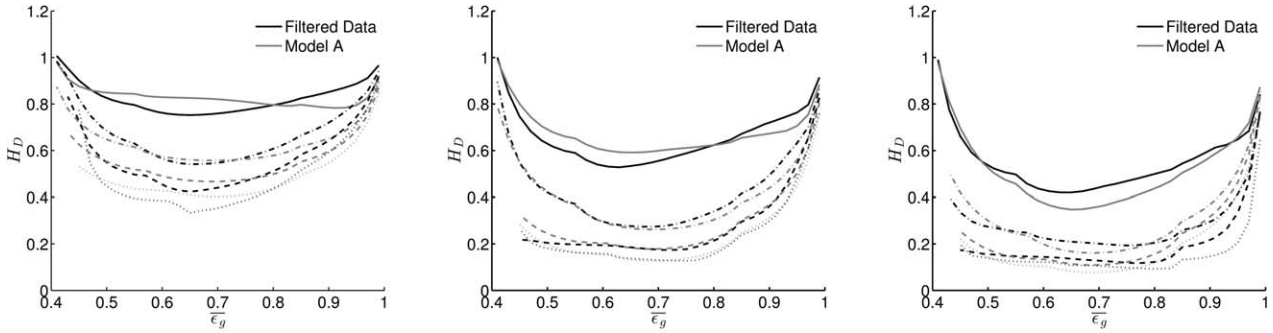

Figure 8. Variation of fits for $H_D = \overline{\beta(u_g - u_s)}/\tilde{\beta}(\tilde{u}_g - \tilde{u}_s)$ with the filtered void fraction, $\bar{\epsilon}_g$, for different dimensionless filter sizes $\hat{\Delta}_f$: — $\hat{\tilde{u}}_{gs} = 0.25$; – · – $\hat{\tilde{u}}_{gs} = 0.75$; – – – $\hat{\tilde{u}}_{gs} = 1.25$; · · · $\hat{\tilde{u}}_{gs} = 1.75$.

$$C_p'(\bar{\epsilon}_s) = 0.17\bar{\epsilon}_s + \frac{0.0235\bar{\epsilon}_s}{\epsilon_s^{max}\left(\epsilon_s^{max} - \bar{\epsilon}_s\right)^{3/4}}$$
$$C_\mu'(\bar{\epsilon}_s) = 0.105\bar{\epsilon}_s + \frac{0.001\bar{\epsilon}_s}{\epsilon_s^{max}\left(\epsilon_s^{max} - \bar{\epsilon}_s\right)} \quad (31)$$

Figure 9 clearly shows that Eq. 31 predicts the values of the filtered pressure and the filtered shear viscosity reasonably well. Especially, this modification (31) yields the correct limits for the filtered solids pressure and the filtered solids shear viscosity as $\bar{\epsilon}_s$ tends to the maximum packing. Finally, a summary of the filtered subgrid modifications is given in Table 2.

Heterogeneity-Based Subgrid Modifications (Model B)

In contrast to Model A, which is directly deduced by using curve fitting of the filtered data, Model B is based on the assumption that the heterogeneity inside fluidized beds is caused by the formation of local clusters. This concept is also supported by experiments (Schneiderbauer et al.[31] and references cited therein). In the case of bubbling fluidized beds, these heterogeneities mostly manifest as clusters-like structures inside bubbles (voids), which has been confirmed recently by experimental and numerical studies.[40–44] Inside (dense phase) and outside (dilute phase) a cluster, the particles are considered as homogeneously distributed. Using these concepts constitutive relations for the effective drag and the effective stresses can be derived.

Heterogeneity-based subgrid drag model (Christian Doppler-Laboratory model)

The CD-Lab (acronym for Christian Doppler-Laboratory) subgrid drag model[31] distinguishes between resolved and unresolved clusters by computing the expectation value of the diameter of the unresolved clusters. Our previous studies[31,45] prove that this subgrid drag modification is well applicable to the coarse grid simulation of bubbling fluidized beds. In particular, this model correctly predicts the bed expansion for a wide range of superficial gas velocities using coarse grids.[45] The CD-Lab subgrid drag model reads

$$\beta^{eff} \equiv \tilde{\beta}^{CL} = \frac{1}{||\tilde{\boldsymbol{u}}_g - \tilde{\boldsymbol{u}}_s||}\left\|\boldsymbol{F}_d^{cl} + f^c \boldsymbol{F}_d^c\right\| \quad (32)$$

In Eq. 32 f^c is the volume fraction of the clusters. $\boldsymbol{F}_d^c$ denotes the drag force per unit volume on the particles in the dense phase. The drag force $\boldsymbol{F}_d^{cl}$ arises from the interaction between the surrounding dilute-phase gas and the particle clusters. In the case of Geldart type B particles, the drag force on the dilute phase particles can be neglected.[28,31] The superscripts c and cl, therefore, refer to the dense phase inside particle clusters and the particle clusters of diameter

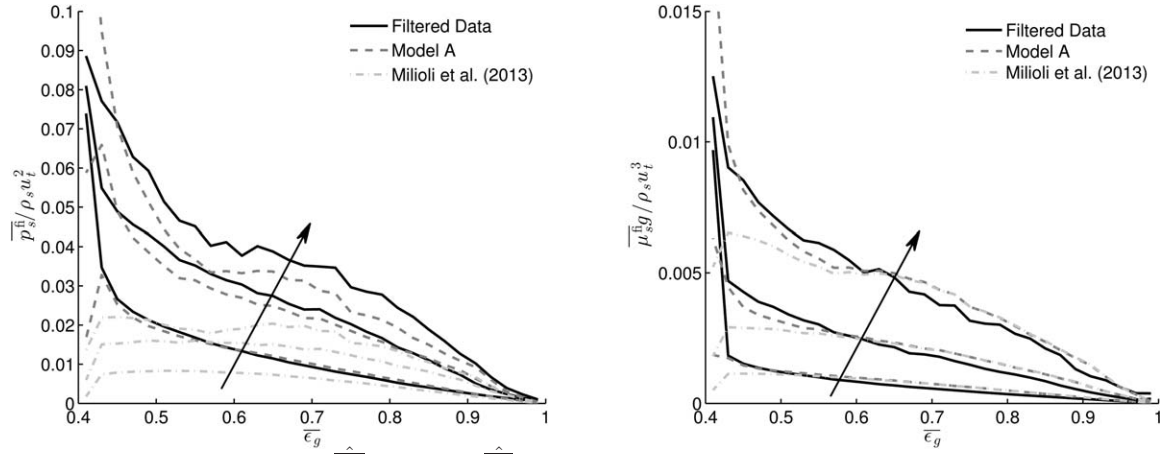

Figure 9. Variation of fits for (a) $\widehat{\overline{p_s^{fi}}}$ and (b) $\widehat{\overline{\mu_s^{fi}}}$ with the filtered void fraction, $\bar{\epsilon}_g$, for different filter sizes $\hat{\Delta}_f \in \{3.74, 7.48, 14.96\}$.

The arrow indicates increasing filter size.

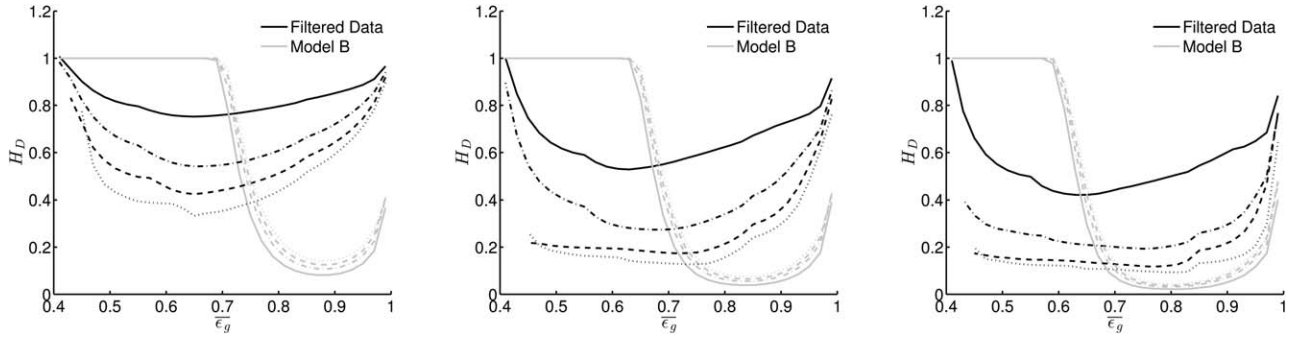

Figure 10. Variation of $H_D^{CL} = \tilde{\beta}^{CL}/\tilde{\beta}$ with the filtered void fraction, $\bar{\epsilon}_g$, for different dimensionless filter sizes $\hat{\Delta}_f$: — $\hat{\tilde{u}}_{gs} = 0.125$; – · – $\hat{\tilde{u}}_{gs} = 0.75$; – – – $\hat{\tilde{u}}_{gs} = 1.25$; · · · $\hat{\tilde{u}}_{gs} = 1.75$.

d_{cl}. For a detailed discussion, the reader is referred to our previous study.[31]

Figure 10 shows the heterogeneity-based subgrid drag modification. The figure reveals that Eq. 32 predicts an opposite dependence on the slip velocity as deduced from the filtered data (Figure 1), that is, H_D^{CL} increases for increasing slip velocity, $\hat{\tilde{u}}_{gs}$. However, the figure clearly demonstrates that the dependency of H_D^{CL} on $\hat{\tilde{u}}_{gs}$ is far less developed than observed from the filtered data. Furthermore, the figure reveals that H_D^{CL} tends to 1 at even higher filtered voidage than the filtered H_D. Nevertheless, H_D^{CL} shows the correct limits ($H_D^{CL} \to 1$) as $\bar{\epsilon}_g$ tends to 1 and as $\bar{\epsilon}_g$ tends to $1-\epsilon_s^{max}$. For large filter length and high slip velocities, H_D^{CL} predicts similar behavior as deduced from the filtered data in dilute regions (Figure 10c). This can be attributed to the closure equations used for the voidage inside of clusters and the cluster diameter (Eqs. 40 and 48 in Schneiderbauer et al.[31]), which were derived from fast fluidization experimental data.[46–48] Therefore, it is remarkably that our previous studies[31,45] clearly demonstrate the applicability of Eq. 32 to coarse grid simulations of bubbling fluidized beds. This can be understood by reviewing Figure 2 yielding that very dense ($\bar{\epsilon}_s \to \epsilon_s^{max}$) and very dilute ($\bar{\epsilon}_s \to 0$) areas are highly likely to occur. In addition, inside of voids the highest slip velocities occur in the fluidized bed. Thus, in both limits Eq. 32 delivers appropriate approximations for the filtered heterogeneity index (e.g., Figure 10c).

Heterogeneity-based SGS model

As mentioned before the solids stress tensor basically consists of two different contributions (kinetic-collisional and frictional parts), which are characterized by different behavior of the interparticle contacts. Figure 4 reveals that in contrast to the inertial regime, in the frictional regime the contribution stemming from the velocity fluctuations appears negligible,[26] whereas the frictional stresses are characterized by subgrid shear layers. These show considerable fluctuations of the shear rate and the solids volume fraction.[8] As both regimes manifest different physics, they require different approaches for the corresponding heterogeneity-based SGS modifications, which we present in the following.

Collisional (Inertial) Stress Model. In the collisional (inertial) regime, which is characterized by heterogenous structures like particle clusters, we, therefore, take up again the cluster concept presented in the previous section. We assume that the contribution from filtered collisional stresses and the Reynolds-stress-like velocity fluctuations, $\overline{\Sigma_s^{fi}}$, can be written as

$$\overline{\Sigma_s^{fi}}(\bar{\epsilon}_s, \rho_s, d_s, \tilde{\Theta}, g_0) = f^c \Sigma_s^{kc}(\epsilon_s^c, \rho_s, d_s, \tilde{\Theta}, g_0^c) + \overline{\Sigma_s^R}(\bar{\epsilon}_s, \rho_s, \Theta^{cl}(d_{cl})) \tag{33}$$

The first term on the right-hand side of Eq. 33 indicates the contribution from the collisions between particles inside a cluster with volume fraction ϵ_s^c (Eq. 40 of Schneiderbauer et al.[31]) and the second term on the right-hand side represents the contribution from the velocity fluctuations at cluster scale. g_0^c denotes the radial distribution function for the particles in clusters and is given by $g_0^c = g_0(\epsilon_s^c)$ (Eq. 59 of Schneiderbauer et al.[31]). Additionally, the expectation value of the cluster diameter d_{cl}, which distinguishes between resolved and unresolved clusters, has been determined by Schneiderbauer et al.[31] (A plot of the cluster diameter d_{cl} as a function of the void fraction ϵ_g can also be found in that study). However, the granular temperature associated with the fluctuation energy of the clusters, Θ^{cl}, appearing in Eq. 33 remains unknown. We, therefore, propose that we can estimate Θ^{cl} from the filtered granular temperature $\tilde{\Theta}$, which is related to the fluctuation energy of the particles inside the clusters. Good approximations for $\tilde{\Theta}$ and Θ^{cl} are[36]

$$\tilde{\Theta} \sim 4||\overline{\mathbf{S}}_s||^2 d_s^2 \quad \text{and} \quad \Theta^{cl} \sim 4||\overline{\mathbf{S}}_s||^2 d_{cl}^2 \tag{34}$$

From above equation, it follows that Θ^{cl} can be written as

$$\Theta^{cl} = h_\Theta(\epsilon_s^c)\left(\frac{d_{cl}}{d_s}\right)^2 \tilde{\Theta} \tag{35}$$

where h_Θ can be determined from the filtered numerical fine grid data. Equation 33 requires that $\overline{\Sigma_s^{fi}}$ approaches $\overline{\Sigma_s^{kc}}$ as d_{cl} tends to zero (i.e., Σ_s^R vanishes) and thus, that the original kinetic theory is recovered in regions of vanishing clusters. Note that clusters may vanish due to a sufficient grid resolution or in the dense regime, where the frictional stresses become dominant.[31] Indeed, Eq. 35 implements theses requirements.

Applying Eq. 33 to the microscopic solids pressure given in Table 3 of Schneiderbauer et al.[31] yields

$$\overline{p_s^{fi}} = \bar{\epsilon}_s \rho_s \left(\frac{1}{1+l_s/\mathbb{L}} + 4\eta_s \epsilon_s^c g_0^c\right)\tilde{\Theta} + \bar{\epsilon}_s \rho_s \Theta^{cl} \tag{36}$$

with $\eta_s = (1+e_s)/2$. Note that the last term on the right-hand side of Eq. 36 accounts for the Reynolds-stress-like velocity

fluctuations, these are the fluctuations at cluster scale. Furthermore, the subgrid modification of the microscopic solids viscosity (Table 3 of Schneiderbauer et al.[31]) is given by

$$\overline{\mu_{\mathrm{s}}^{\mathrm{fi}}}=\left(\frac{2+\alpha}{3}\right)\left\{\frac{f^{\mathrm{c}}\mu^{*}}{g_0^{\mathrm{c}}\eta_{\mathrm{s}}(2-\eta_{\mathrm{s}})}\left(\frac{1}{1+\frac{l_{\mathrm{s}}}{\mathbb{L}}}+\frac{8}{5}\epsilon_{\mathrm{s}}^{\mathrm{c}}\eta_{\mathrm{s}}g_0^{\mathrm{c}}\right)\left(1+\frac{8}{5}\eta_{\mathrm{s}}(3\eta_{\mathrm{s}}-2)\epsilon_{\mathrm{s}}^{\mathrm{c}}g_0^{\mathrm{c}}\right)+\frac{3}{5}\eta_{\mathrm{s}}\mu_b^{\mathrm{c}}\right\}+\overline{\mu_{\mathrm{s}}^{\mathrm{R}}},\tag{37}$$

where

$$\mu_c^{\mathrm{c}}=\frac{8}{3}\bar{\epsilon}_{\mathrm{s}}\rho_{\mathrm{s}}\sqrt{\frac{\tilde{\Theta}}{\pi}}\epsilon_{\mathrm{s}}^{\mathrm{c}}d_{\mathrm{s}}g_0^{\mathrm{c}}\tag{38}$$

and

$$\mu^{*}=\frac{\mu}{1+\frac{2\tilde{\beta}^{\mathrm{CL}}\mu}{(\epsilon_{\mathrm{s}}^{\mathrm{c}}\rho_{\mathrm{s}})^2g_0^{\mathrm{c}}\tilde{\Theta}}},\quad \mu=\frac{5\rho_{\mathrm{s}}d_{\mathrm{s}}\sqrt{\pi\tilde{\Theta}}}{96},\quad \alpha=\frac{8}{5}$$

The contribution from the Reynolds-stress-like velocity fluctuations can be estimated according to Eqs. 19, 34, and 36 yielding

$$\overline{\mu_{\mathrm{s}}^{\mathrm{R}}}\approx\frac{\bar{\epsilon}_{\mathrm{s}}\rho_{\mathrm{s}}\Theta^{\mathrm{cl}}}{2||\bar{\mathbf{S}}_{\mathrm{s}}||}=\bar{\epsilon}_{\mathrm{s}}\rho_{\mathrm{s}}d_{\mathrm{cl}}\sqrt{\Theta^{\mathrm{cl}}}$$

In addition, the term $\boldsymbol{q}$ (Table 3 of Schneiderbauer et al.[31]) has also to be transformed according to Eq. 33 reading

$$\overline{\boldsymbol{q}^{\mathrm{fi}}}=-\frac{\kappa^{*}}{g_0^{\mathrm{c}}}\left\{f^{\mathrm{c}}\left(\frac{1}{1+\frac{l_{\mathrm{s}}}{\mathbb{L}}}+\frac{12}{5}\eta_{\mathrm{s}}\epsilon_{\mathrm{s}}^{\mathrm{c}}g_0^{\mathrm{c}}\right)\left(1+\frac{12}{5}\eta_{\mathrm{s}}^2(4\eta_{\mathrm{s}}-3)\epsilon_{\mathrm{s}}^{\mathrm{c}}g_0^{\mathrm{c}}\right)+\frac{64}{25\pi}(41-33\eta_{\mathrm{s}})\eta_{\mathrm{s}}^2\bar{\epsilon}_{\mathrm{s}}\epsilon_{\mathrm{s}}^{\mathrm{c}}(g_0^{\mathrm{c}})^2\right\}\nabla\tilde{\Theta}\tag{39}$$

where

$$\kappa^{*}=\frac{\kappa}{1+\frac{6\tilde{\beta}^{\mathrm{CL}}\kappa}{5(\epsilon_{\mathrm{s}}^{\mathrm{c}}\rho_{\mathrm{s}})^2g_0^{\mathrm{c}}\tilde{\Theta}}},\quad \kappa=\frac{75\rho_{\mathrm{s}}d_{\mathrm{s}}\sqrt{\pi\tilde{\Theta}}}{48\eta_{\mathrm{s}}(41-33\eta_{\mathrm{s}})}$$

Frictional (Interial) Stress Model. In the frictional regime, the situation renders differently compared to the collisional regime, as the subgrid heterogeneity is characterized by the formation of shear bands instead of clusters. To derive an expression for the subgrid modification of the frictional pressure, $p_{\mathrm{s}}^{\mathrm{fr}}$ (Table 3 of Schneiderbauer et al.[31]), we start from the definition of its filtered counterpart

$$\overline{p_{\mathrm{s}}^{\mathrm{fr}}}(\boldsymbol{x})=\iiint p_{\mathrm{s}}^{\mathrm{fr}}(\boldsymbol{y})G_{\Delta}(\boldsymbol{x}-\boldsymbol{y})d\boldsymbol{y}\tag{40}$$

where G_{Δ} denotes a weighting function normalized to unity. We now assume that the filtered frictional pressure, $\overline{p_{\mathrm{s}}^{\mathrm{fr}}}$, can be deduced from the formation of subgrid shear bands in the frictional regime, which yields

$$\overline{p_{\mathrm{s}}^{\mathrm{fr}}}(\boldsymbol{x})\approx\sum_{\mathrm{sb}\in\mathcal{S}}p_{\mathrm{s}}^{\mathrm{fr}}(\boldsymbol{y}_{\mathrm{sb}})G_{\Delta}(\boldsymbol{x}-\boldsymbol{y}_{\mathrm{sb}})\tag{41}$$

where $\mathcal{S}$ denotes the set of all shear bands. In the case of the discretized TFM equations, $G_{\Delta}(\boldsymbol{x}-\boldsymbol{y}_{\mathrm{sb}})$ is the box filter given with radius Δ. However, in Eq. 40, the unresolved frictional pressure, $p_{\mathrm{s}}^{\mathrm{fr}}$, is unknown as it depends on the unresolved variables ϵ_{s} and $||\mathbf{S}_{\mathrm{s}}||$. Thus, these variables are decomposed into mean, that is, filtered ($\bar{}$), and spatially fluctuating ($'$) components

$$\begin{aligned}\epsilon_{\mathrm{s}}&=\overline{\epsilon_{\mathrm{s}}}+\epsilon_{\mathrm{s}}^{'},\\ D_{\mathrm{s},ij}&=\overline{D_{\mathrm{s},ij}}+D_{\mathrm{s},ij}^{'},\end{aligned}\tag{42}$$

where the $D_{\mathrm{s},ij}$'s are the components of the rate-of-deformation tensor $\mathbf{D}_{\mathrm{s}}$. Following,[8] it is reasonable to assume that $D_{\mathrm{s},ij}^{'}$ follows a Normal distribution $\mathcal{N}(0,\sigma_{\mathbf{D},ij}^2)$ with the standard deviation

$$\sigma_{\mathbf{D},ij}=\delta\frac{\sqrt{\tilde{\Theta}}}{d_{\mathrm{s}}}\tag{43}$$

where δ is a constant of the order unity. In the frictional regime, it is found that $\delta\approx 1/4$.[8] Furthermore, we propose that $\epsilon_{\mathrm{s}}^{'}$ can be approximated by a Normal distribution $\mathcal{N}(0,\sigma_{\epsilon}^2)$, where σ_{ϵ}^2 is given by (correlated from experimental data[31,46,47])

$$\sigma_{\epsilon}=(\epsilon_{\mathrm{s}}^{\max}-\bar{\epsilon}_{\mathrm{s}})(0.002+1.48\bar{\epsilon}_{\mathrm{s}}+0.79\bar{\epsilon}_{\mathrm{s}}^2-4.67\bar{\epsilon}_{\mathrm{s}}^3)\tag{44}$$

Finally, Savage[8] suggested that usually the thickness of shear layers, d_{sb}, is found to be of the order of 10 particle diameters. Then, Eq. 41 can be evaluated by using, for example, a Monte Carlo method yielding

$$\overline{p_{\mathrm{s}}^{\mathrm{fr}}}\approx\frac{1}{\bar{\Delta}_{\mathrm{sb}}}\sum_{k=1}^{\bar{\Delta}_{\mathrm{sb}}}p_{\mathrm{s}}^{\mathrm{fr}}(\epsilon_{\mathrm{s},k},||\mathbf{S}_{\mathrm{s},k}||),\tag{45}$$

with $\bar{\Delta}_{\mathrm{sb}}=\Delta/d_{\mathrm{sb}}$, $d_{\mathrm{sb}}\approx 10d_{\mathrm{s}}$ and $||\mathbf{S}_{\mathrm{s},k}||=\sqrt{\mathbf{S}_{\mathrm{s},k}:\mathbf{S}_{\mathrm{s},k}/2}$. In Eq. 45, $\epsilon_{\mathrm{s},k}$ and $S_{\mathrm{s},ij,k}=D_{\mathrm{s},ij,k}-(1/3)D_{\mathrm{s},ll,k}\delta_{ij}$ are normally distributed random numbers according to Eqs. 42–44.

Similar to the frictional pressure, it is straightforward to define the effective frictional viscosity accounting for subgrid shear layers as follows

$$\overline{\mu_{\mathrm{s}}^{\mathrm{fr}}}\approx\frac{1}{\bar{\Delta}_{\mathrm{sb}}}\sum_{k=1}^{\bar{\Delta}_{\mathrm{sb}}}\mu_{\mathrm{s}}^{\mathrm{fr}}(\epsilon_{\mathrm{s},k},||\mathbf{S}_{\mathrm{s},k}||)\tag{46}$$

Finally, a summary of the heterogeneity based subgrid modifications is given in Table 3.

Discussion. In this section, we compare the heterogeneity-based subgrid modifications for the solids pressure and the solids shear viscosity with the corresponding filtered data. Because, the flux of PTE is generally negligible in bubbling fluidized beds,[9] we abstain from a more detailed discussion of the closure for $\overline{\boldsymbol{q}^{\mathrm{fi}}}$. In Figure 11, the heterogeneity-based SGS modifications as a function of the filtered void fraction for

$$h_{\Theta}(\epsilon_{\mathrm{s}}^{\mathrm{c}})=0.15\sqrt{\frac{\epsilon_{\mathrm{s}}^{\mathrm{c}}}{\epsilon_{\mathrm{s}}^{\max}}}$$

are plotted. It appears that Eqs. 36, 45, 37, and 46 show reasonable agreement with the filtered pressure data in the case of small filter lengths. Especially, the frictional subgrid modifications (Eqs. 45 and 37) yield the correct limits as $\bar{\epsilon}_{\mathrm{s}}$ tends to $\epsilon_{\mathrm{s}}^{\max}$. However, for large filter lengths the heterogeneity-based SGS corrections considerably underestimate the filtered solids stresses around $\bar{\epsilon}_{\mathrm{g}}=0.5$ as the form of Θ^{cl} underestimates the contribution of the Reynolds-stress-like velocity fluctuations in this case (this is attributed to the functional form of d_{cl}, see Figure 2 in Schneiderbauer

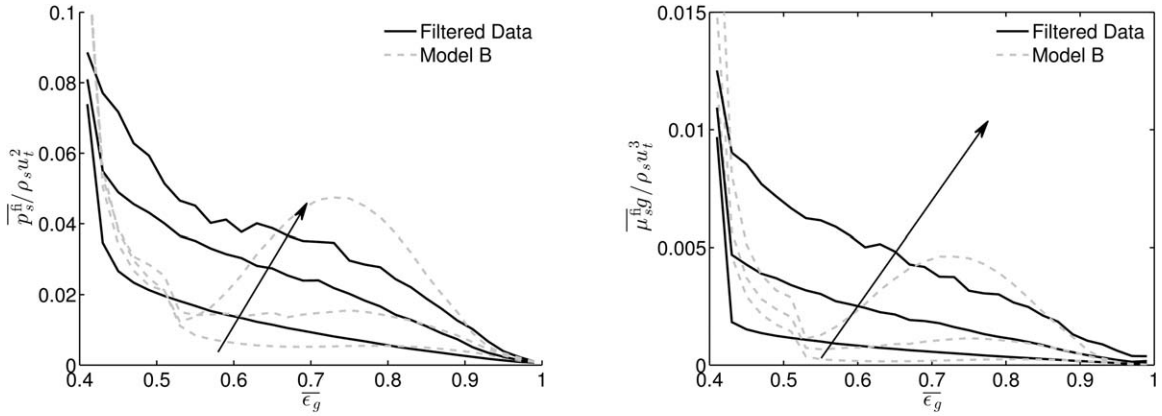

Figure 11. Variation of heterogeneity-based (a) $\widehat{\overline{p_s^{fi}}}$ and (b) heterogeneity-based $\widehat{\overline{\mu_s^{fi}}}$ with the filtered void fraction, $\bar{\epsilon}_g$, for different filter sizes $\hat{\Delta}_f \in \{3.74, 7.48, 14.96\}$.

The arrow indicates increasing filter size.

et al.[31]). Furthermore, Figure 11b indicates that Θ^{cl} does not show the appropriate behavior in the limit of large filter sizes, which, in turn, is a consequence of the model assumptions. On the one hand, we have assumed that the subgrid heterogenous structures manifest as spherical clusters in dilute areas. Conversely, the void fraction inside these clusters has been supposed to be constant. These assumptions are reasonable for small filter lengths as demonstrated by Figure 11 but for large filter lengths clusters may itself contain heterogenous substructures and, therefore, the subgrid corrections accounting for the Reynolds-stress-like velocity fluctuations are less accurate. In contrast, close the maximum packing the frictional SGS correction, which is based on the formation of subgrid shear band, appears to be insensitive to the filter length. To conclude, the heterogeneity-based SGS corrections yield the correct limits as $\bar{\epsilon}_s$ tends to ϵ_s^{max} and as $\bar{\epsilon}_s$ tends to 0, respectively. These modifications seem, therefore, to be applicable to bubbling fluidized beds as voids and very dense regions prevail (compare with Figure 2).

Verification of Subgrid Modifications

In the following, we verify the presented subgrid modifications (Tables 2 and 3) in the case of coarse grid simulations of the bubbling fluidized bed used to generate the fine grid data (see Figure 4 and Table 2 in Schneiderbauer et al.[31]). For this purpose, we compare time averaged global properties, such as bed expansion and bubble statistics, obtained from the coarse grid simulations with the fine grid simulation.

Solids phase distribution

In Figure 12a, a comparison of the time-averaged axial profile of the filtered solids volume fraction $\bar{\epsilon}_s$ for $\hat{W}_g^{in}=0.22$ is plotted. The figure shows that the computed bed expansion and solids phase distribution obtained on coarse grids is in fairly good agreement with the reference simulation, which is additionally indicated by Figure 13. Remarkably, although both subgrid modifications (Models A and B) show different dependencies on the filtered drag and the filtered slip

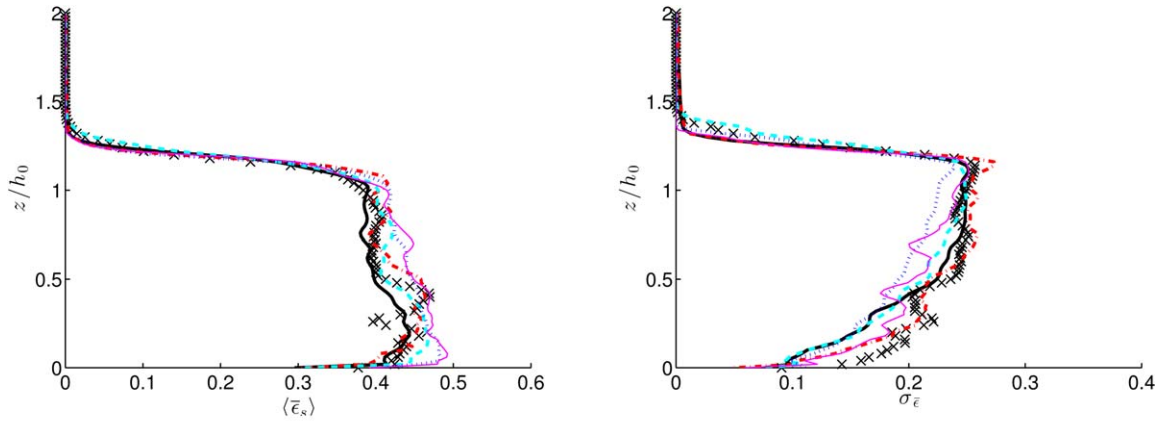

Figure 12. Axial profiles (i.e., $x=y=0$) of the time averaged filtered solids volume fraction, $\langle\bar{\epsilon}_s\rangle$, and its standard deviation, $\sigma_{\bar{\epsilon}}$, for $\hat{W}_g^{in}=0.22$ (the averaging time is 10 s): ··· (blue line color) Model A using $\hat{\Delta}=7.48$; — (magenta) Model A using $\hat{\Delta}=3.74$; — (black line) Model B using $\hat{\Delta}=7.48$; – · – (red line) Model B using $\hat{\Delta}=3.74$; – – – (cyan color) Model B without SGS modifications using $\hat{\Delta}=7.48$;(ref 31) $\times\beta_{WY}$ using $\hat{\Delta}=0.93$ ($\equiv$ fine grid).

[Color figure can be viewed in the online issue, which is available at wileyonlinelibrary.com.]

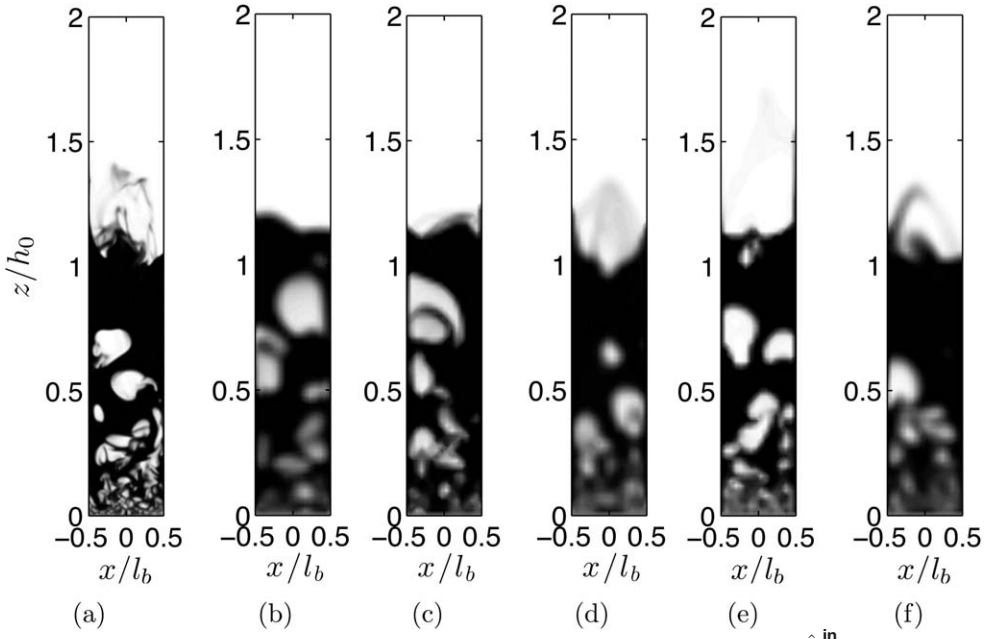

Figure 13. Snapshots of the filtered solids volume fraction, $\bar{\epsilon}_s$, at $t = 10$ s for $\hat{W}_g^{in} = 0.22$ (white: $\epsilon_s = 0$; black: $\epsilon_s = \epsilon_s^{max}$).

(a) fine grid, (b) Model A using $\hat{\Delta} = 7.48$, (c) Model A using $\hat{\Delta} = 3.74$, (d) Model B using $\hat{\Delta} = 7.48$, (e) Model B using $\hat{\Delta} = 3.74$, (f) Model B without SGS using $\hat{\Delta} = 7.48$.[31] l_b (= 150 mm) denotes the length of the bed.

velocity, they predict the bed expansion precisely and yield similar bubble patterns (Figure 13). This can be explained by reviewing Figure 2, which yields that very dilute regions, that is, bubbles, and very dense areas are most likely to occur. On the one hand, inside those voids high slip velocities are observed, which are of $\mathcal{O}(u_t)$. The filtered drag data shows only a negligible dependence on the slip velocity for large filter sizes in this case and Model B, therefore, reveals reasonable agreement with the filtered correlations (Figure 10). Conversely, in very dense regions the filtered drag data as well as Model B reveal that H_D approaches unity, that is, no drag correction is applied in those areas. Thus, Model B is able to predict the particle distribution in bubbling fluidized beds reasonably well although it appears that it does not correspond to the filtered drag data for intermediate volume fractions (which occur very rarely).

Exemplarily, we further examine the impact of applying SGS modifications in the case of Model B. It is observed that the SGS modifications have only little influence on the solids phase distribution and the bed expansion as the magnitude of the drag is much larger than the particle stresses.[23] Thus, the bed expansion is mainly triggered by the drag force and nearly insensitive to the magnitude of the particle stresses. The figure also reveals that the presented models appear insensitive to the grid resolution.

In Figure 12b, the standard deviation, $\sigma_{\bar{\epsilon}}$, of the time-averaged filtered solids volume fraction is plotted. The standard deviation gives evidence whether the coarse grid simulations reveal as distinct bubbles as the resolved simulation[31] (compare also with Figure 13). It appears that each coarse grid simulation (with and without SGS modifications in the case of Model B) yields as distinct bubbles as the reference simulation. Remarkably, even the filtered subgrid modifications (Model A) reveal those distinct bubbles, which is in contrast to the filtered constitutive relations of Igci et al.[26] as shown by our previous study.[31] It appears that solely slip velocity dependent drag corrections are able to deliver sharp distinct bubbles. However, more simulations using, for example, the new revised version of the drag modification of Igci et al., which has been presented by Milioli et al.,[27] are required to substantiate this observation. To conclude, the appearance of the bubbles is triggered mostly by the drag force, which has also been discussed in Schneiderbauer et al.[31] extensively.

Particle mass flux

Figure 14 shows the variations of the corresponding dimensionless filtered solids mass flux, which is made dimensionless using a characteristic solid flux, $q_s^{ch} = \epsilon_s^{max} \rho_s u_t$.[49] It is observed that the computed mass fluxes on the coarse grid simulations are in reasonable agreement with the resolved simulation. Similar to the resolved case, the coarse grid simulations yield rising particles in the center of the bed and slowly downward flowing particles in the dense side region (not shown here). However, Model A generally underpredicts the upward particle flux in the center of the bed. The horizontal profiles (not shown here) indicate that gas-solid flow is not symmetric in this case. Although in the case of Model B and the fine grid simulation the maximum of the particle flux tends to the left, in the case of Model A, the maximum tends to the right. Nevertheless, the solids flow is in reasonable agreement with the fine grid simulation.

Finally, Figure 14 also reveals that the solids flow is not affected by the subgrid contribution of the particle stresses in the case of Model B and that it is determined by the magnitude of the drag force.[31] Furthermore, the presented modifications show no considerable grid dependency.

Bubble size, number density, and rise velocity

Finally, we may ask whether the coarse grid simulations including SGS modifications are able to predict the mean bubble diameters, the bubble density, and the bubble rise velocity

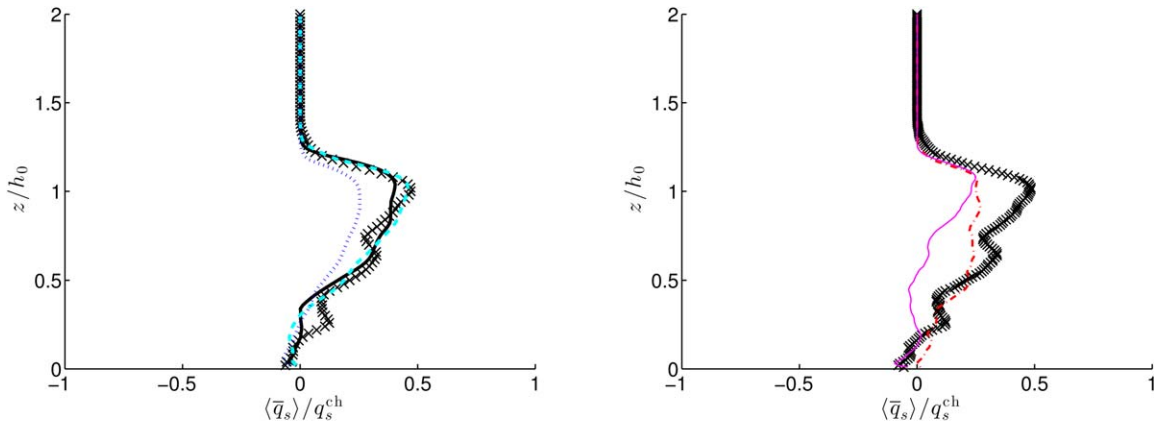

Figure 14. Axial profiles (i.e., $x = y = 0$) of the filtered time averaged dimensionless particle mass flux in vertical direction, $\langle \overline{q_s} \rangle / q_s^{ch}$, for $\hat{W}_g^{in} = 0.22$ and different coarse grid resolutions.

The lines and symbols have the same meaning as in Figure 12. [Color figure can be viewed in the online issue, which is available at wileyonlinelibrary.com.]

precisely. Thus, we evaluate the bubble properties via digital image analysis of the volume fraction maps of the center plane. The methodology follows the procedure presented in our previous study.[31] Thus, we do not repeat the details here.

In Figure 15, the corresponding dimensionless mean bubble diameter as a function of the normalized height z/h_0 is plotted, whereas Figure 16 shows the bubble number density as a function of the bubble diameter. Remarkably, the coarse grid simulations accounting for the contribution of the SGSs reveal nearly identical bubble statistics as obtained from the coarse grid simulation omitting SGS effects (in the case of Model B). The figure clearly shows that each coarse grid case yields a fairly good estimate of the bubble number density and the bubble size distribution (within the spread of the fine grid simulation data).

In Figure 17, the dimensionless bubble rise velocity as a function of the bubble diameter is plotted. Our previous study [31] confirmed that the bubble rise velocities obtained from the highly resolved simulation are in fairly good agreement with the empirical correlation of Hilligardt and Werther.[50] However, the coarse grid simulations without consideration for the SGSs in the frictional regime (– – –; only evaluated in the case of Model B) considerably overestimate the rise velocity of the bubbles although the size of the bubbles is consistent with the resolved simulation. Even though accounting for the subfilter-scale Reynolds-stress-like velocity fluctuations (− · −) does not deliver suitable bubble rise velocities. This has also been shown in our previous study[31] using the SGS closures of the group of Sundaresan.[26] Thus, it can be concluded that the bubble rise velocities are insensitive to these

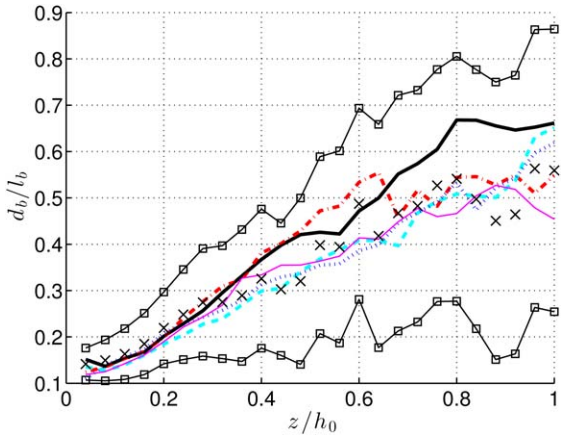

Figure 15. Dimensionless mean bubble diameter as a function of the normalized height, z/h_0, for $\hat{W}_g^{in} = 0.22$ (sampling time is 10 s).

l_b denotes the width of the bed. The lines and symbols have the same meaning as in Figure 12. −□− denotes the spread of the bubble diameter obtained from fine grid simulation. [Color figure can be viewed in the online issue, which is available at wileyonlinelibrary.com.]

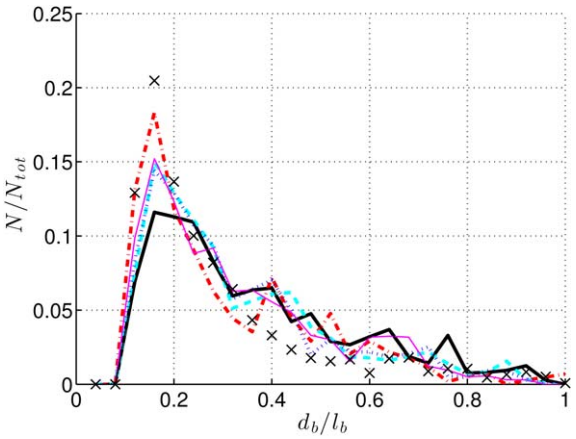

Figure 16. Normalized bubble number density as a function of the normalized mean bubble diameter, d_b/b, for $\hat{W}_g^{in} = 0.22$ (sampling time is 10 s).

l_b denotes the width of the bed. The lines and symbols have the same meaning as in figure 12. [Color figure can be viewed in the online issue, which is available at wileyonlinelibrary.com.]

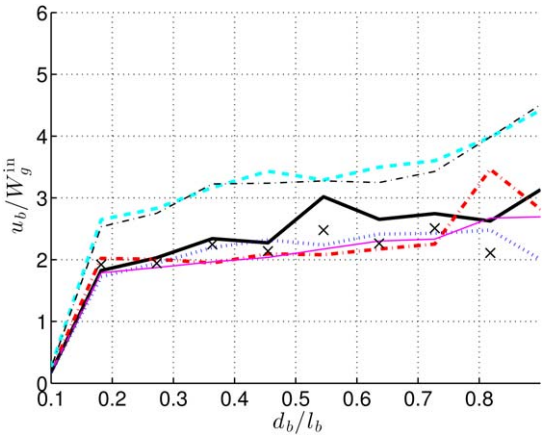

Figure 17. Dimensionless bubble rise velocity, u_b/W_g^{in}, as a function of the normalized bubble diameter, d_b/b, for $\hat{W}_g^{in}$ =0.22 (sampling time is 10 s).

l_b denotes the width of the bed. The lines and symbols have the same meaning as in Figure 12. [Color figure can be viewed in the online issue, which is available at wileyonlinelibrary.com.]

velocity fluctuations. In detail, the raw data (not shown here) suggests that primarily the rise velocities of the larger bubbles are substantially overpredicted by these coarse grid simulations. This, in turn, implies that the countercurrently downflowing layer of particles around these larger bubbles[51] is not resolved adequately. In contrast, applying the presented SGS modifications including the frictional contribution (—, – · –, · · ·, and —) yield fairly good agreement of the bubble rise velocity with the reference simulation.

It is important to emphasize that in the case of coarse grids the bubble rise velocity can only be estimated precisely by considering the subgrid contribution to the frictional stresses. Furthermore, the computed bubble rise velocities are quite insensitive to the grid resolution for the presented SGS modifications.

Conclusions

We have introduced two new closures for the heterogeneity index H_D, that is the correction of a homogenous drag correlation to account for subgrid structures, and we have presented two new constitutive relations for the unresolved parts of the solids stresses. The first model (Model A) is directly deduced from the filtered data by using curve fitting. The second model (Model B) is derived based on the assumption of the formation of subgrid heterogeneities inside fluidized beds. In contrast to EMMS, which is also fundamentally based on the cluster concept, the heterogeneity-based model distinguishes between resolved and unresolved clusters.

The models have been verified on the one hand, against filtered data and conversely, in the case of coarse grid simulations of a pseudo-two-dimensional bubbling fluidized bed with $\hat{W}_g^{in}$ =0.22 and two different coarse grid resolutions. The results are discussed with respect the fine grid reference simulation. This study reveals that:

a. The filtered drag force shows a considerable dependence on the filtered slip velocity and on the filtered solids volume fraction.
b. In dilute areas, the filtered stresses are dominated by an unresolved contribution stemming from Reynolds-stress-like velocity fluctuations. However, even at intermediate filtered solids volume fractions the filtered frictional stresses show a nonnegligible contribution, which has not been taken into consideration by prior studies.[6,26,27] Similar to Milioli et al.,[27] the filtered solids stresses can be described by a Smagorinsky-like subgrid model.
c. The presented subgrid modifications, which are deduced from the filtered data, yield appropriate behavior for a wide range of filtered solids volume fractions, filtered slip velocities, filtered shear rates, and filter lengths.
d. The heterogeneity-based subgrid modifications reveal at least appropriate behavior in very dilute and very dense regions, which are most likely to occur in bubbling fluidized beds.
e. Although Model B (especially the frictional stress modification) can easily applied to different constitutive relations, material properties, and simulation cases,[45] Model A is strongly connected to the setup used for the fine grid simulations. Thus, for a different setup it may be necessary to repeat the fine grid simulations to adapt the filtered residual correlations.
f. Nevertheless, the contribution from the SGSs has minor impact on the hydrodynamics of the fluidized bed. Especially, bed expansion, solids phase distribution, gas flow, particle mass flux, and bubble sizes are insensitive to the magnitude of the particle stresses.
g. Applying the presented subgrid modifications yields fairly good agreement of the stresses near the maximum packing and, therefore, the correct rise velocity of bubbles and slugs. Hence, a SGS modification for the frictional stresses is indispensable to estimate the bubble rise velocity in bubbling fluidized beds precisely.
h. The results further prove that the presented modifications are insensitive to the grid resolution.
i. Compared to the resolved simulation the computational demand is reduced by approximately two orders of magnitude using the coarse grid for equal time step sizes. Coarse meshes, however, allow larger time steps that additionally improve the computational efficiency by approximately one order of magnitude in our study. As no additional equation for the PTE is required in the case of Model A, the computational demand is additionally reduced by a factor 2.5.

To conclude, this study demonstrates that the presented subgrid modifications apply well to the coarse grid simulation of a bubbling fluidized bed of fine particles. However, several tasks remain. First, it is necessary to verify these correlation on even coarser grids, which particularly links to the heterogeneity-based corrections. Second, the range of validity for different fluidized bed setups in the case of Model A has to be determined. Third, the models should also be validated at large scale fluidized beds ($\mathcal{O}(10)$m). Thus, the general validity of the models must be further investigated and the differences to the drag relation of Milioli et al.[27] have to be explained. These will be addressed in future publications.

Acknowledgments

This work was funded by the Christian-Doppler Research Association, the Austrian Federal Ministry of Economy, Family and Youth, and the Austrian National Foundation for

Research, Technology and Development. The authors thank Prof. Sankaran Sundaresan and Stefan Radl for many useful discussions and helpful comments.

Notation

Latin symbols

$\mathbf{D}_s$ = rate of deformation tensor for solid phase
d_s = particle diameter
d_{cl} = cluster diameter
e_s = coefficient of restitution
Fr = particle-based Froude number
f^c = volume fraction of clusters
g_0 = radial distribution function
g = gravitational acceleration
H_D = heterogeneity index
$\mathbf{I}$ = identity tensor
I_s = inertial number (Table 3 of Schneiderbauer et al.[31])
$\mathbb{L}_{ch}$ = characteristic length scale of subgrid heterogeneities
$\mathbb{L}$ = characteristic length scale of the domain
l_s = mean free path of the particles (Table 3 of Schneiderbauer et al.[31])
p_s^{fr} = solids pressure due to friction
p_s^{kc} = solids pressure due kinetic and collisional contributions
$\boldsymbol{q}$ = flux of PTE
$\boldsymbol{\Sigma}_s$ = stress tensor associated with the particle phase
$\boldsymbol{\Sigma}_s^{fr}$ = frictional contribution to $\boldsymbol{\Sigma}_s$
$\boldsymbol{\Sigma}_s^{kc}$ = kinetic and collisional contributions to $\boldsymbol{\Sigma}_s$
$\boldsymbol{u}_g, \boldsymbol{u}_s$ = local average velocity of gas and particle phase, respectively
$\boldsymbol{u}_{gs}$ = local average of the gas-solid slip velocity
u_t = terminal settling velocity
W_g = superficial gas velocity in vertical direction

Greek symbols

β = interphase drag coefficient
Δ = grid spacing
Δ_f = filter size
Δ_{sb} = width of a shear band
ϵ_g = volume fractions of gas phase
ϵ_s = volume fractions of solid phase
ϵ_s^{max} = maximum packing ratio
γ_Θ = rate of dissipation of PTE by inelastic collisions
λ_s^{kc} = solids bulk viscosity from KTGF
μ_s = solids viscosity
μ_s^{fr} = frictional contribution to μ_s
μ_s^{kc} = kinetic and collisional contributions to μ_s
$\boldsymbol{\phi}_p$ = unresolved part of the buoyancy
$\boldsymbol{\phi}_D$ = unresolved part of the drag
ρ_s = densities of solid
Θ = granular temperature

Superscripts

c = cluster
cl = cluster fluctuation
fi = filtered
fr = frictional
kc = kinetic-collisional
R = Reynolds-stress like velocity fluctuations

Accents

$\sim$ = Favre averaged variable
- = filtered variable
^ = dimensionless variable

Literature Cited

1. Xue Q, Heindel TJ, Fox RO. A CFD model for biomass fast pyrolysis in fluidized-bed reactors. *Chem Eng Sci.* 2011;66(11):2440–2452.
2. Lyngfelt A, Leckner B, Mattisson T. A fuidized-bed combustion process with inherent CO2 separation; application of chemical-looping combustion. *Chem Eng Sci.* 2001;56:3101–3113.
3. Hatzantonis H, Yiannoulakis H, Yiagopoulos A, Kiparissides C. Recent developments in modeling gas-phase catalyzed olefin polymerization fluidized-bed reactors: the effect of bubble size variation on the reactor's performance. *Chem Eng Sci.* 2000;55:3237–3259.
4. Fernandes FAN, Lona LMF. Heterogeneous modeling for fluidized-bed polymerization reactor. *Chem Eng Sci.* 2001;56:963–969.
5. Rokkam RG, Fox RO, Muhle ME. Computational fluid dynamics and electrostatic modeling of polymerization fluidized-bed reactors. *Powder Technol.* 2010;203(2):109–124.
6. Igci Y, Andrews AT, Sundaresan S, Pannala S, O'Brien T. Filtered two-fluid models for fluidized gas-particle suspensions. *AIChE J.* 2008;54(6):1431–1448.
7. Milioli CC, Milioli FE. On the subgrid behavior of accelerated riser flows for a high stokes number particulate. *Ind Eng Chem Res.* 2011;50(23):13538–13544.
8. Savage SB. Analyses of slow high-concentration flows of granular materials. *J Fluid Mech.* 1998;377:1–26.
9. van Wachem BGM, Schouten JC, van den Bleek CM, Krishna R, Sinclair JL. Comparative analysis of CFD models of dense gas-solid systems. *AIChE J.* 2001;47(5):1035–1051.
10. Almuttahar A, Taghipour F. Computational fluid dynamics of high density circulating fluidized bed riser: study of modeling parameters. *Powder Technol.* 2008;185(1):11–23.
11. Reuge N, Cadoret L, Coufort-Saudejaud C, Pannala S, Syamlal M, Caussat B. Multifluid Eulerian modeling of dense gas-solids fluidized bed hydrodynamics: influence of the dissipation parameters. *Chem Eng Sci.* 2008;63(22):5540–5551.
12. Schneiderbauer S, Aigner A, Pirker S. A comprehensive frictional-kinetic model for gas-particle flows: analysis of fluidized and moving bed regimes. *Chem Eng Sci.* 2012;80:279–292.
13. Anderson TB, Jackson R. Fluid mechanical description of fluidized beds. Equations of motion. *Ind Eng Chem Fundam.* 1967;6(4):527–539.
14. Ishii M. Thermo-fluid dynamic theory of two-phase flow. Collection de la Direction des Etudes et recherches d'Electricité de France. Paris: Eyrolles, 1975.
15. Batchelor GK. Secondary instability of a gas-fluidized bed. *J Fluid Mech.* 1993;257:359–371.
16. Glasser BJ, Kevrekidis IG, Sundaresan S. One- and two- dimensional travelling wave solutions in fluidized beds. *J Fluid Mech.* 1996;306:183–221.
17. Glasser BJ, Kevrekidis IG, Sundaresan S. Fully developed travelling wave solutions and bubble formation in fluidized beds. *J Fluid Mech.* 1997;334:157–188.
18. Andrews AT, Loezos PN, Sundaresan S. Coarse-grid simulation of gas-particle flows in vertical risers. *Ind Eng Chem Res.* 2005;44(16):6022–6037.
19. Li T, Grace J, Bi X. Study of wall boundary condition in numerical simulations of bubbling fluidized beds. *Powder Technol.* 2010;203(3):447–457.
20. Koenigsdorff R, Werther J. Gas-solids mixing and flow structure modeling of the upper dilute zone of a circulating fluidized bed. *Powder Technol.* 1995;82:317–329.
21. Xu G, Li J. Multi-scale interfacial stresses in heterogeneous particle-fluid systems. *Chem Eng Sci.* 1998;53(18):3335–3339.
22. Agrawal K, Loezos PN, Syamlal M, Sundaresan S. The role of meso-scale structures in rapid gas-solid flows. *J Fluid Mech.* 2001;445:151–185.
23. Parmentier JF, Simonin O, Delsart O. A functional subgrid drift velocity model for filtered drag prediction in dense fluidized bed. *AIChE J.* 2012;58(4):1084–1098.
24. Wang J. A review of Eulerian simulation of geldart A particles in gas-fluidized beds. *Ind Eng Chem Res.* 2009;48:5567–5577.
25. Lu B, Wang W, Li J. Searching for a mesh-independent sub-grid model for CFD simulation of gas-solid riser flows. *Chem Eng Sci.* 2009;64(15):3437–3447.
26. Igci Y, Sundaresan S. Constitutive models for filtered two-fluid models of fluidized gas-particle flows. *Ind Eng Chem Res.* 2011;50(23):13190–13201.
27. Milioli CC, Milioli FE, Holloway W, Agrawal K, Sundaresan S. Filtered two-fluid models of fluidized gas-particle flows: new constitutive relations. *AIChE J.* 2013;59(9):3265–3275.
28. Wang J, van der Hoef MA, Kuipers JAM. Coarse grid simulation of bed expansion characteristics of industrial-scale gas-solid bubbling fluidized beds. *Chem Eng Sci.* 2010;65(6):2125–2131.
29. Schneiderbauer S, Schellander D, Pirker S. A filtered frictional-kinetic model for gas-solid fluidized and moving beds. In: Witt PJ, editor. *Proceedings of the 9th International Conference on CFD in the Minerals and Process Industries.* Melbourne, Australia: CSIRO, 2012: 7.

30. Sarkar A, Sun X, Sundaresan S. Sub-grid drag models for horizontal cylinder arrays immersed in gas-particle multiphase flows. *Chem Eng Sci*. 2013;104:399–412.
31. Schneiderbauer S, Puttinger S, Pirker S. Comparative analysis of subgrid drag modifications for dense gas-particle flows in bubbling fluidized beds. *AIChE J*. 2013;59(11):4077–4099.
32. Zhang DZ, VanderHeyden WB. The effects of mesoscale structures on the macroscopic momentum equations for two-phase flows. *Int J Multiphase Flow*. 2002;28(5):805–822.
33. Lun CKK, Savage SB, Jeffrey DJ, Chepurniy N. Kinetic theories for granular flow: inelastic particles in Couette flow and slightly inelastic particles in a general flowfield. *J Fluid Mech*. 1984;140:223–256.
34. Wen CY, Yu YH. Mechanics of fluidization. *Chem Eng Prog Symp Ser*. 1966;62:100.
35. Wang W, Li J. Simulation of gas-solid two-phase flow by a multi-scale CFD approach – of the EMMS model to the sub-grid level. *Chem Eng Sci*. 2007;62(1–2):208–231.
36. Sundaresan S, Radl S, Milioli CC, Milioli FE. Coarse-grained models for momentum, energy and species transport in gas-particle flows. *The 14th International Conference on Fluidization From Fundamentals to Products, edited by ECI Symposium Series*, 2013. Noordwijkerhout, The Netherlands: Engineering Conferences International, NY, 2013:8.
37. Smagorinsky J. General circulation experiments with the primitive equations. *Mon Weather Rev*. 1963;91:99–164.
38. Schneiderbauer S, Puttinger S, Pirker S. Validation of sub-grid modifications for dense gas-particle flows in case of a pseudo-2D bubbling fluidized bed. Proceedings of the 8th International Conference on Multiphase Flow. Jeju, Korea: ICMF, 2013:8.
39. Schneiderbauer S, Pirker S. A frictional-kinetic model for dilute to dense gas-particle flows. In: Eberhardsteiner J, Böhm HJ, Rammerstorfer FG, editors. CD-ROM Proceedings of the 6th European Congress on Computational Methods in Applied Sciences and Engineering (ECCOMAS 2012). Vienna, Austria: Vienna University of Technology, 2012:14.
40. Laverman JA, Roghair I, Van Sint Annaland M, Kuipers JAM. Investigation into the hydrodynamics of gas-solid fluidized beds using particle image velocimetry coupled with digital image analysis. *Can J Chem Eng*. 2008;86(3):523–535.
41. Busciglio A, Vella G, Micale G, Rizzuti L. Analysis of the bubbling behaviour of 2D gas solid fluidized beds part I. Digital image analysis technique. *Chem Eng J*. 2008;140(1–3):398–413.
42. van der Hoef MA, van Sint Annaland M, Deen NG, Kuipers JAM. Numerical simulation of dense gas-solid fluidized beds: a multiscale modeling strategy. *Ann Rev Fluid Mech*. 2008;40(1):47–70.
43. Goldschmidt MJV, Link JM, Mellema S, Kuipers JAM. Digital image analysis measurements of bed expansion and segregation dynamics in dense gas-fluidised beds. *Powder Technol*. 2003;138(2–3):135–159.
44. Taghipour F, Ellis N, Wong C. Experimental and computational study of gas-solid fluidized bed hydrodynamics. *Chem Eng Sci*. 2005;60(24):6857–6867.
45. Schneiderbauer S, Pirker S. A coarse-grained two-fluid model for gas-solid fluidized beds. *J Comput Multiphase Flows*. In press.
46. Bai D, Issangya AS, Grace JR. Characteristics of gas-fluidized beds in different flow regimes. *Ind Eng Chem Res*. 1999;38(3):803–811.
47. Issangya AS, Grace JR, Bai D, Zhu J. Further measurements of flow dynamics in a high-density circulating fluidized bed riser. *Powder Technol*. 2000;111(1–2):104–113.
48. Zou B, Li H, Xia Y, Ma X. Cluster structure in a circulating fluidized bed. *Powder Technol*. 1994;78:173–178.
49. Igci Y, Sundaresan S. Verification of filtered two-fluid models for gas-particle flows in risers. *AIChE J*. 2011;57(10):2691–2707.
50. Hilligardt K, Werther J. Local bubble gas hold-up and expansion of gas/solid fluidized beds. *Ger Chem Eng*. 1986;9(4):215–221.
51. Botterill JSM, George JS, Besford H. Bubble chains in gas fluidized beds. *Chem Eng Prog Symp Ser*. 1966;62(62):7–14.

Manuscript received Sept. 12, 2013, and revision received Dec. 7, 2013.